UNIVERSITÀ DEGLI STUDI DI PADOVA

Dipartimento di Fisica e Astronomia "Galileo Galilei"

Master Degree in Nuclear Physics

Final Dissertation

Study of Exotic Nuclei with GRIFFIN.

Thesis supervisor

Prof. Silvia Monica Lenzi

Thesis co-supervisor

Dr. Bruno Olaizola Mampaso

Candidate

Hassan, Khwaja Idrees

Academic Year 2022/2023

Acknowledgment

I would like to take this opportunity to express my heartfelt gratitude to the individuals and institutions that have been instrumental in the completion of my master's degree and this thesis.

First and foremost, I am deeply thankful to my thesis advisor, **Dr. Bruno Olaizola**, whose unwavering support, guidance, and expertise have been the driving force behind this research endeavor. Your mentorship has not only enriched my academic experience but has also inspired me to strive for excellence.

My profound appreciation goes to the Erasmus Mundus Joint Master degree program in Nuclear Physics and the European Agency for Culture and Education (EACEA) for providing the financial support that made my academic pursuit possible. This scholarship has not only granted me access to world-class education but has also broadened my horizons in the field of Nuclear Physics.

I extend my sincere thanks to my internship supervisor, **François de Oliveira** at GANIL, and my colleague, **Laurie Dienis** for their assistance and support during the course of my degree. Your contributions, both academically and personally, have been deeply meaningful.

In addition, I am very grateful to all my professors from the University of Seville, Complutense University of Madrid, Autonomous University of Madrid, the University of Barcelona, and Caen-Normandy University for their exceptional teaching, mentorship, and contributions to my academic growth.

I wish to acknowledge and extend my heartfelt gratitude to all those who lent a helping hand during the course of my degree. Your support, whether academic or personal, has been invaluable and greatly appreciated.

And to my family, I owe an immeasurable debt of gratitude. Your unwavering support, encouragement, and understanding throughout the challenges and successes of my academic journey have been a constant source of strength.

I dedicate my master's degree to my beloved parents, whose unwavering love, support, and sacrifices have been the driving force behind my educational journey. Your boundless encouragement, guidance, and belief in me have shaped not only my academic achievements but also my character. This degree is a testament to your dedication as a parent and your enduring commitment to my success. With all my love and gratitude!

Abstract

The experiment S1723 conducted at the ISAC facility at TRIUMF, Canada, involves the generation of RIB using the ISOL technique. A proton beam [Svensson and Garnsworthy, 2014]is employed to induce various nuclear reactions, such as spallation, fragmentation, and fission, in suitable target materials, resulting in a wide range of isotopes. Among these, ^{62}Mn is produced via the fission process. To selectively isolate specific isotope species from this mixture, RILIS technology is utilized. RILIS employs a precisely tunable narrow-band laser to selectively excite and ionize target atomic or isotopic species. Subsequently, a potential difference accelerates the ionized isotopic species with energies between 20 keV and 40 keV [Garnsworthy et al., 2019]. The isotopes are then directed to the ISOL mass separator, where magnetic forces separate and isolate the desired isotope, in this case, ^{62}Mn [Kunz et al., 2023, Baartman, 2014, Raeder et al., 2013].

The ^{62}Fe isotope was studied via the decay of ^{62}Mn using the GRIFFIN spectrometer, comprising 16 high-purity germanium (HPGe) clover-type detectors, augmented by auxiliary detection systems. This thesis presents a detailed construction of a new level scheme for ^{62}Fe, in comparison to previous reports [Runte et al., 1983] and [Hoteling et al., 2010]. The analysis includes the identification of new transitions and excited states, as well as the calculation of log ft values for observed transitions and states, and suggests new spin-parity for the new levels.

List of Figures

List of Tables

Contents

List of acronyms

GRSISort	Gamma-Ray Spectroscopy at ISAC
HPGe	High Purity Germanium
N-N Interaction	Nucleon-Nucleon Interaction
ESPE	Effective Single-Particle Energy
ISOL	Isotope Separation On-Line
ISAC	Isotope Separator and Accelerator
RIB	Radioactive Ion Beam
RILS	Resonance Ionization LASER Ion
TRIUMF	Tri-University Meson Facility
GRIFFIN	Gamma-Ray Infrastructure For Fundamental Investigations of Nuclei
DAQ	Data Acquisition
DESCANT	DEuterated SCintillator Array for Neutron Tagging
SCEPTAR	SCintillating Electron-Positron Tagging Array
LaBr3(Ce)	Lanthanum Bromide with Cerium dopant
TIGRESS	TRIUMF ISAC Gamma-Ray Escape-Suppressed Spectrometer
BGO	Bismuth Germanate ($Bi_4Ge_3O_{12}$)
NNDC	National Nuclear Data Center

Chapter 1
Thesis Overview

Exotic nuclei, often referred to as exotic isotopes or radioactive nuclei, represent a unique class of atomic nuclei that diverge from the conventional configurations observed in stable elements. They are characterized by an excess of either protons or neutrons, which results in a pronounced imbalance within their nuclear composition. These nuclei are situated far from the stability region on the nuclear chart and typically exhibit short lifetimes due to their inherent instability and hence may have different structural properties from the stable nuclei. The foundation of our understanding of nuclear structure, particularly in stable nuclei, lies in the concept of magic numbers. In the nuclear shell model, each nucleon, whether a neutron or a proton, moves within a mean potential influenced by its interactions with other nucleons. This potential results in the formation of nuclear shells, which represent quantized energy levels where nucleons are situated. The most stable nuclei are those that have completely filled or closed shells, leading to the emergence of what we call "magic numbers". In the realm of stable nuclei at the Valley of Stability, these magic numbers are 8, 20, 28, 50, 82, and 126, signifying particularly stable and well-defined nuclear configurations [Otsuka et al., 2020].

Over the years, experimental studies have revealed that the well-established concept of magic numbers in nuclear structure becomes less clear when examining exotic nuclei, particularly those far from stability. Exotic nuclei, with nucleon numbers that would typically be considered magic, do not always exhibit the expected properties. When additional nucleons are introduced to or removed from stable nuclei, the energies of single particles are altered, and strong quadrupole correlations emerge. These correlations can disrupt the usual spherical mean-field shell gaps, leading to the preference for energetically favorable deformed intruder configurations, sometimes even becoming the ground states. Consequently, the conventional sequence of orbital arrangements can be inverted (known as the island of inversion), causing the disappearance of known magic numbers and the emergence of new ones. The island of inversion was initially observed in the N = 8 nucleus, ^{11}Be [Alburger et al., 1964], and has since been extensively explored in various regions of the nuclide chart. One notable example is the Island of Inversion surrounding ^{32}Mg, particularly near the neutron shell closure N = 20 [Thibault et al., 1975]. These structural transformations are believed to be influenced by changes in the strength of the spin-orbit coupling [Dobaczewski et al., 1994] and the significant proton-neutron interactions prevalent in neutron-rich nuclei [Otsuka et al., 2005].

Extensive experimental and theoretical investigations have been undertaken to examine the nuclear structure of neutron-rich nuclei located near Z = 28 and N = 40. These studies aim to deepen our understanding of the distinct characteristics exhibited by nuclei in this region, characterized by a notable excess of neutrons.

The interplay between spherical and collective configurations holds special significance in the study of neutron-rich nuclei below Z = 28 and N = 40. Within the framework of the harmonic oscillator potential, N = 40 is regarded as a magic number. However, this magic character is tempered by the influence of the spin-orbit interaction, which results in the lowering of orbitals with the highest angular momentum (j) in the succeeding major oscillator shell, specifically the $g_{9/2}$ orbital in this context. As a consequence, the excitation energy of the E(2_1^+) state in ^{68}Ni is notably high, exceeding 2 MeV, and

the B(E2) transition rate is the lowest in the region. This interplay between structural factors adds complexity to the behavior of these neutron-rich nuclei [Fraile-Prieto et al., 2008].

Neutron-rich isotopes of Fe and Cr around N = 40, the neutron $0g_{9/2}$ orbital, located close to the *pf*-shell ($0f_{5/2}$, $1p_{3/2}$, and $1p_{1/2}$) that has a negative parity, plays a paramount role. Despite its relatively smaller angular momentum (j), this specific neutron orbital assumes a central role in driving strong collectivity and instigating structural changes within this segment of the nuclear chart. Its influence extends to the formation of nuclear isomers characterized by half-lives spanning several orders of magnitude [Fraile-Prieto et al., 2008].
Additionally, the occupation of the proton $0f_{7/2}$ orbital, transitioning from Cr to Fe and subsequently to Ni, leads to modifications in the relative energies of negative parity pf neutron orbitals. These alterations arise from the potent and attractive neutron-proton tensor interaction, further amplifying the complexity of behaviors observed in these nuclei [Li, 2023].

The goal in the present thesis is to study ^{62}Fe which is produced from the decay of ^{62}Mn via β^- decay. In Chapter 2, we discuss the Island of Inversion, including the disappearance of conventional magic numbers and the emergence of novel ones. Chapter 3 explores the physics behind beta decay. Chapter 4 emphasizes the experimental aspects, including various detectors used in the research. Chapter 5 discusses the experiment. Chapter 6 provides a detailed account of the analysis and presents the research findings.

Chapter 2
Introduction

2.1 Island of inversion

One of the essential nuclear models is the Nuclear Shell Model which describes the arrangements of nucleons in discrete energy levels within the nucleus as analogous to the atomic model. Nuclei with "magic numbers" of protons and neutrons such as 2, 8, 20, 28, 50, 82, and 126 tend to be more stable and exhibit higher binding energies due to completely filled nuclear shells [Krane, 1991]. See Fig. 2.1.

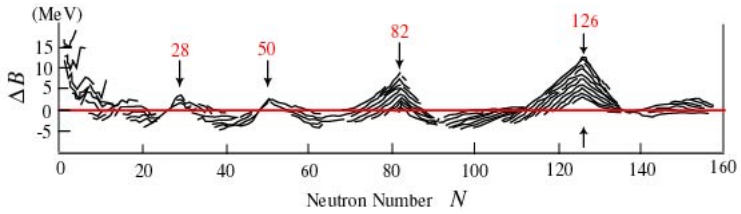

Figure 2.1: *Deviations of the experimental binding energies from the values of the Weizsaecker-Bethe Mass Formula [mag,].*

However, one of the drawbacks of the nuclear shell model is the island of inversion [Brown, 2010]. Islands of Inversion have been observed or predicted at N = 8, 14, 28, 40, and 50 [Alburger et al., 1964,Navin et al., 2000,Bastin et al., 2007,Adrich et al., 2008,Stanoiu et al., 2008,Naimi et al., 2012,Li, 2023,Nowacki et al., 2016].

2.2 Island of inversion around N = 40

Current research efforts, both in terms of experiments and theories, have been directed towards exploring the region with N = 40 in the island of inversion [Brown, 2010] and even extended to N = 50 [Nowacki et al., 2016]. The emergence of an island of inversion near the N = 40 region is substantiated by the outcomes derived from theoretical investigations documented in [Lenzi et al., 2010,Gaudefroy et al., 2009] as well as from the experimental observations presented in [Adrich et al., 2008,Ljungvall et al., 2010,Pauwels et al., 2008]. The increase in collectivity noticed at around N = 40 is attributed to the presence of neutrons occupying intruder states from a higher shell, reminiscent of the island of inversion phenomenon seen around N = 20. Although N = 40 is not traditionally regarded as a shell closure within the shell model, [Bernas et al., 1982] proposed the concept of its magicity. Following the discovery of a high-lying first excited state in ^{68}Ni, its presence was confirmed through measurements carried out by [Broda et al., 1995]. The closed-shell characteristic of N = 40 received additional support when researchers measured the reduced transition probability B(E2; $2^+ \rightarrow 0^+$) in ^{68}Ni, resulting in the smallest B(E2) value among all semi-magic nuclides [Sorlin et al., 2002]. The N = 40 shell closure is understood to be weak, especially when the atomic number (Z) is below 28. This is because, below Z = 28, the interaction between protons and neutrons begins to have a significant influence on the occupancy of nucleon orbitals (specifically $\nu f_{5/2}$ and $\nu g_{9/2}$), and as a result, it also affects the total binding energy of the nucleus [Naimi et al., 2012]. Studies involving β-decay in neutron-rich isotopes of Titanium (Ti), Vanadium (V), Chromium (Cr), Manganese (Mn), and Iron

(Fe) [Bernas et al., 1991, Hannawald et al., 1999, Sorlin et al., 1999, Sorlin et al., 2003a, Gaudefroy et al., 2005, Pauwels et al., 2009, Daugas et al., 2011] have shown that the dominant component in the allowed Gamow-Teller β-decay process is the transition from $\nu f_{5/2}$ to $\pi f_{7/2}$. The presence of neutrons in the intruder orbital $\nu g_{9/2}$ is strongly influenced by the interplay between protons and neutrons. This interaction weakens when protons are taken out from the $\pi f_{7/2}$ orbital, causing the $\nu f_{5/2}$ orbital to move closer to the $\nu g_{9/2}$ orbital. In this proximity, the pairing effect encourages the scattering of pairs to higher orbits, as observed in various studies [Sorlin et al., 2002, Gaudefroy et al., 2005, Grzywacz et al., 1998, Sorlin et al., 2003b, Grawe et al., 2001].

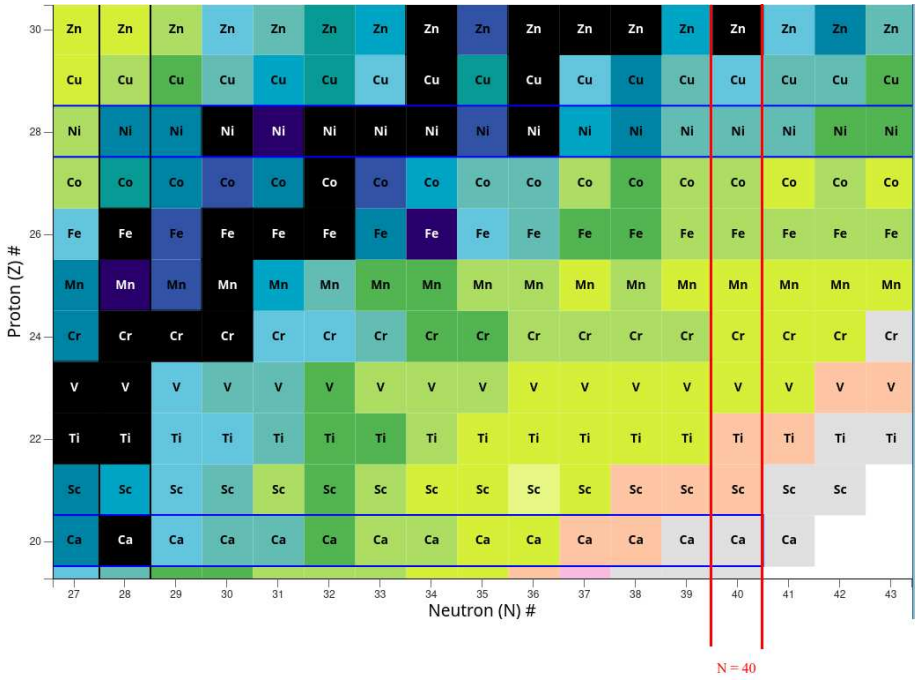

Figure 2.2: *$1p_{\frac{3}{2}}$, $0f_{\frac{5}{2}}$, $1p_{\frac{1}{2}}$ orbitals below $N = 40$ and $0g_{\frac{9}{2}}$ orbital beyond $N = 40$ [nnd,].*

2.2.1 Shell Evolution

The evolution of the shell structure is not only influenced by the nuclear forces which is referred to as Type I shell evolution. Shell structure is also influenced by to proton-neutron tensor force combined with the nuclear forces, referred to as Type II shell evolution [Tsunoda et al., 2014].
The makeup of exotic nuclei, which exhibit extreme proportions of protons (Z) to neutrons (N), presents distinct structural characteristics. In [Otsuka et al., 2005], explains how the structure of the nucleus changes because of the tensor force. This force comes from the way protons and neutrons interact with each other, which was explained by Yukawa [Yukawa, 1935] for the first time, using meson exchange processes. The tensor force is a unique part of this interaction and shows its connection to meson exchange. The tensor force is given as

$$V_T = (\vec{\tau}_1 \cdot \vec{\tau}_2) \left([\vec{s}_1 \, \vec{s}_2]^{(2)} \cdot Y^{(2)} \right) f(r) \tag{2.1}$$

Here $\vec{\tau}_{1,2}$ and $\vec{s}_{1,2}$ represent the isospin and spin of the the nucleons 1 and 2, respectively. Where f(r) is a function of relative distance. $\vec{s}_1$ and $\vec{s}_2$ are the dipole operators coupled to rank 2. Y is the spherical harmonics for the Euler angles of the relative coordinate [Otsuka et al., 2005]. To better understand the properties of individual particles inside a nucleus, we can use the so-called effective single-particle energies (ESPEs). These ESPEs show us how the presence of other particles in the nucleus influences a single particle in a specific orbit. The interaction matrix depends on the J-dependence, i.e., the angular momentum of the two interacting nucleons (j and j$'$) [Otsuka, 2002], the interaction is given as

$$V^{T}_{jj'} = \frac{\sum_J (2J+1)\,\langle jj'|V|jj'\rangle_{JT}}{\sum_J (2J+1)} \tag{2.2}$$

The interaction matrix has J-dependence and since we are dealing with the mean effect, the J-dependency is averaged with a weight factor of 2J + 1, and only the diagonal matrix elements are considered. If neutrons are occupying the j$'$ orbit and protons the j orbit, then the shift of the energy is given as

$$\Delta\epsilon_p(j) = \frac{1}{2}\{V^{T-0}_{jj'} + V^{T-1}_{jj'}\}n_n(j') \tag{2.3}$$

similarly

$$\Delta\epsilon_i(j) = \frac{1}{2}\{V^{T-0}_{jj'} + V^{T-1}_{jj'}\}n_i(j') \quad \text{where i can be a proton or neutron} \tag{2.4}$$

In the above Equation 2.4, $n_i j'$ are the number of protons (or neutrons). $\Delta\epsilon_i$ is the change of the single-particle energy as a function of j.
If protons and neutrons share the same orbital, the change in ESPE becomes somewhat more complex due to the considerations of isospin symmetry [Bansal and French, 1964]. We begin with an example illustrated in Fig. 2.3. Protons occupy either $j_> = l + 1/2$ or $j_< = l$ - 1/2 states, while neutrons are found in either $j'_> = l' + 1/2$ or $j'_< l'$ - 1/2 states, where l and l' being the angular momenta. These particular orbits correspond to either valence states or hole states in close proximity to the Fermi surface. To simplify matters, their radial wave functions are determined using the harmonic oscillator potential.

Treating the V as a tensor force, the orbits j and j$'$ satisfy the following identity

$$(2j_> + 1)\,V^{T}_{j_> j'} + (2j_< + 1)\,V^{T}_{j_< j'} = 0 \tag{2.5}$$

Since this identity is in the isospin formalism and can be applied in two different cases, (i) between protons and neutrons, like the case in Fig. 2.3(a). (ii) The exchange processes responsible for the monopole interaction induced by the tensor force. 2.3(b). Additionally, the same characteristic is also applicable to a spin-spin central interaction [Otsuka et al., 2001]. Here, where only exchange terms are taken into account, the spin-coordinate components of the T = 0 and T = 1 matrix elements exhibit an opposite behavior.

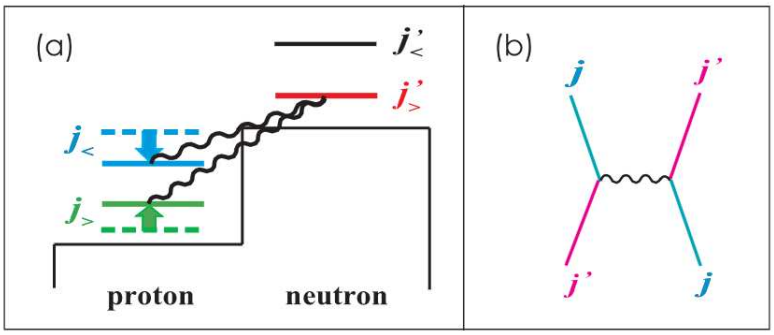

Figure 2.3: *(a) Visual representation of the monopole interaction generated by the tensor force, involving a proton with $j_{>,<} = l \pm 1/2$ and a neutron with $j'_{>,<} = l' \pm 1/2$ states. (b) The exchange processes involved in the monopole interaction arise from the tensor force. [Otsuka et al., 2005].*

As it was just mentioned that the redial wave functions are given by the harmonic oscillator potential, the validity of Equation 2.2 could be compromised if either the single-particle state $j_>$ or $j_<$ happens to match j', due to the impact of isospin symmetry on the summation of substates. However, in reality, the monopole matrix elements tend to follow the pattern described in Equation 2.5, at least to some extent. It can be demonstrated that when either j or j' equals $s_{1/2}$, $V^{T}_{j,j'}$ becomes zero. Equation 2.5 hints that if both $j_>$ and $j_<$ orbital states are entirely occupied, their collective tensor monopole effect disappears.

By combining the two isospins in Equation 2.1, we get

$$V^{T=0}_{j,j'} = 3 \times V^{T=1}_{j,j'} \quad \text{for } j \neq j' \tag{2.6}$$

Therefore, it can be concluded that the proton-neutron tensor monopole interaction carries twice the strength of the T = 1 interaction.

The key question is how the tensor force affects ESPEs and whether there is a consistent rule governing this influence. It can be explained through Fig. 2.4.

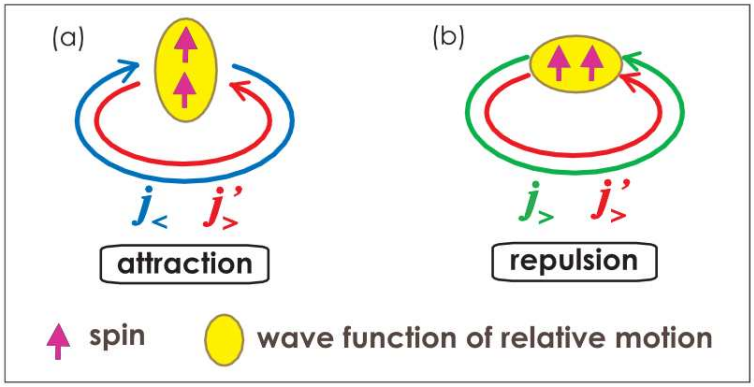

Figure 2.4: *An illustrative representation of the tensor force's influence on two nucleons occupying orbits denoted as j and j'. [Otsuka et al., 2005].*

In Fig. 2.4(a), shows a scenario in which a nucleon from the $j_<$ orbital interacts with another nucleon residing in the $j'_>$ orbital. Due to their significantly high relative momentum, the spatial wave function describing their relative motion becomes highly concentrated along the direction of their collision, which coincides with the orbital motion direction. In this specific configuration, the spins of the two nucleons align in a parallel fashion, resulting in an overall spin state of S = 1. This phenomenon closely resembles the behavior observed in the case of the deuteron, where the tensor force exerts an attractive effect. The same underlying mechanism applies when considering two nucleons in $j_>$ and $j'_<$ orbits. Conversely, as illustrated in Figure 2.4(b), the tensor force exerts a repulsive influence when acting upon two nucleons located in $j_>$ and $j'_>$ orbits (or the other way around). This repulsion arises from the stretching of the wave function describing their relative motion along the collision direction. Consequently, we can establish a clear framework in which $j_>$ and $j'_>$ orbits (or the other way around) are mutually attractive, whereas $j_>$ and $j'_>$ (or $j_<$ and $j'_<$) exhibit mutual repulsion.

Fig. 2.5 illustrates the triplet-even potential arising from the tensor force within various potential models, including π exchange, $\pi + \rho$ exchange, M3Y [Bertsch et al., 1977], AV8′ [Pudliner et al., 1997], and the G matrix (GM) appropriate for typical nuclear densities.

The first two potentials are established based on standard meson-nucleon coupling constants [Osterfeld, 1992, Bäckman et al., 1985]. While notable differences are observed in the short-distance region, these potentials exhibit limited variation for distances beyond 0.8 fm, with the exception of

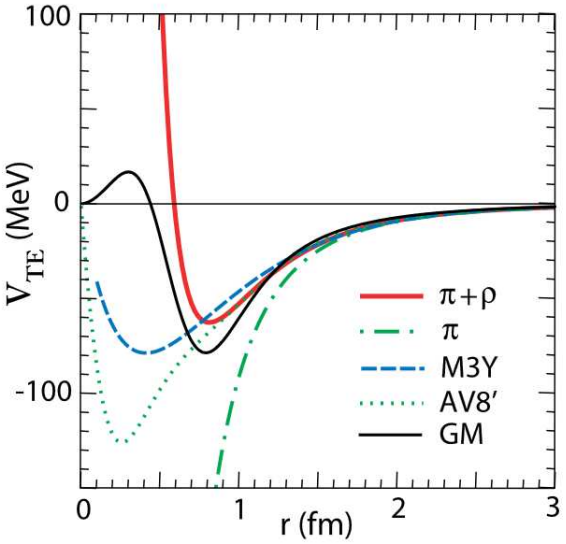

Figure 2.5: *The triplet-even potential resulting from the tensor force as calculated within multiple interaction models. [Otsuka et al., 2005].*

π exchange. To simplify matters, a chosen potential with an appropriate radial (inner) cutoff at 0.7 fm is employed. Intriguingly, all these interaction models, except for π exchange, yield remarkably similar results. Given the AV8′ interaction's ability to accurately replicate the properties of the deuteron [Pudliner et al., 1997], it is reasonable to conclude that the current treatment of the tensor force aligns effectively with the structural characteristics of the deuteron. Additional details about shell evolution are presented in Reference [Otsuka et al., 2020]

Chapter 3
Theory

3.1 Radioactivity

In the field of nuclear physics, we come across numerous isotopes, each having its unique combination of protons and neutrons, which gives them distinct properties like mass and half-life. However, it is important to note that most of these combinations are not stable. Instead, they tend to release energy or particles as they try to become more stable [Krane, 1991].

Nuclei can go through various decay processes, mainly α, β, γ decay, and spontaneous fission. Spontaneous fission tends to occur in heavy nuclei, causing them to split into two large parts and release several free neutrons. α decay involves the emission of an α ($^4_2$He) particle, which is a tightly bound cluster of two protons and two neutrons. This process is governed by a strong nuclear force and shares similarities with spontaneous fission. On the other hand, β decay is a different process where a nucleus transforms a proton into a neutron or vice versa, emitting a β particle and either a neutrino or an anti-neutrino. β decay is driven by the weak interaction. An additional phenomenon within weak interactions is known as Electron Capture (EC), sharing similarities with β^+ decay. However, in this process, an atomic electron is captured, contrasting with β^+ decay, which involves the emission of a β^+ particle. Following are the Feynman diagrams for the three types of beta decay are shown in Fig. 3.1, 3.2, and 3.3 [Krane, 1991].

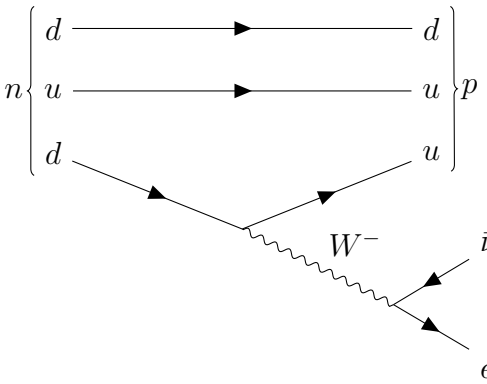

Figure 3.1: *Neutron decay via β^- to proton [fey,]. The Direction of time is from left to right. In β^- the neutron number decreases by one unit.*

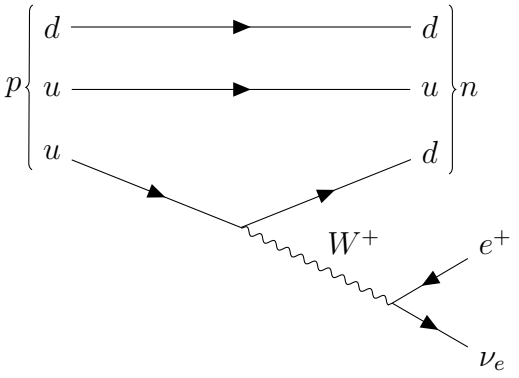

Figure 3.2: *Proton decay via β^+ to neutron [fey,]. The Direction of time is from left to right. In β^+ the proton number decreases by one unit.*

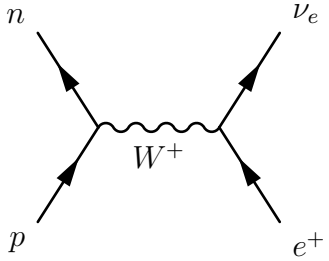

Figure 3.3: *Electron capture shown through Feynman diagram [fey,]. The Direction of time is from left to right. In EC the proton number decreases by one unit.*

Decay processes in nuclear physics are typically expressed as follows:

α decay :

$$ {}^{A}_{Z}X_N \longrightarrow {}^{A-4}_{Z-4}X_{N-2} + \alpha $$

β^+ decay :

$$ {}^{A}_{Z}X_N \longrightarrow {}^{A}_{Z-1}X_{N+1} + e^+ + \nu_e $$

β^- decay :

$$ {}^{A}_{Z}X_N \longrightarrow {}^{A}_{Z+1}X_{N-1} + e^- + \bar{\nu_e} $$

Electron Capture :

$$ {}^{A}_{Z}X_N + e^- \longrightarrow {}^{A}_{Z-1}X_{N+1} + \nu_e $$

These spontaneous decay processes all depend on a fundamental requirement: the energy or particles present in the initial reactants must have more mass-energy than the resulting products. This difference in mass energy is simply referred to as the Q-value. In the case of the decay methods we discussed above, we can express these Q-values through the following expressions [Krane, 1991].

$\mathbf{Q}_\alpha$:

$$ M\left({}^{A}_{Z}X_N\right)c^2 - M\left({}^{A-4}_{Z-4}X_{N-2}\right)c^2 - M\left(\alpha\right)c^2 $$

$\mathbf{Q}_{\beta^+}$:

$$ M\left({}^{A}_{Z}X_N\right)c^2 - M\left({}^{A}_{Z-1}X_{N+1}\right)c^2 - 2m_e c^2 $$

$\mathbf{Q}_{\beta^-}$:

$$ M\left({}^{A}_{Z}X_N\right)c^2 - M\left({}^{A}_{Z+1}X_{N-1}\right)c^2 $$

$\mathbf{Q}_{EC}$:

$$M\left({}^{A}_{Z}X_{N}\right)c^{2} \; - \; M\left({}^{A}_{Z+1}X_{N-1}\right)c^{2}$$

3.2 Radioactive Decay Law

Nuclear decay is a random process, and during very short time intervals (dt), the probability of decay remains constant. The number of radioactive nuclei (dN) that decay during a time interval (dt) is proportional to the decay constant (λ) multiplied by the number of nuclei in the sample (N) at that specific time (t) [Krane, 1991].

$$dN = -\lambda N(t)dt \tag{3.1}$$

Where

$$\lambda = \frac{ln2}{t_{1/2}} \tag{3.2}$$

λ being the decay constant and $t_{1/2}$ is the half life of the nuclei.

The lifetime (τ) associated with an excited state is mathematically expressed as the inverse of the decay constant (λ). This lifetime signifies the time required for the number of nuclei within a sample to decrease by a factor of 1/e. Furthermore, the exponential law that characterizes the process of radioactive decay can be derived through the integration of Equation 3.1.

$$N(t) = N_o\, e^{-\lambda t} \; = \; N(0)\, e^{-ln2\cdot t/t_{1/2}} \tag{3.3}$$

3.3 Allowed β-decay

This section explores the theory of β-decay, drawing upon the insights and principles outlined in Reference [Grotz and Klapdor, 1990].

Before discussing the allowed β-decay, let's introduce Pauli spin matrices and the ladder operators.

$$\boldsymbol{\sigma}_1 = \begin{pmatrix} 0 & 1 \\ 1 & 0 \end{pmatrix} \tag{3.4}$$

$$\boldsymbol{\sigma}_2 = \begin{pmatrix} 0 & -\iota \\ \iota & 0 \end{pmatrix} \tag{3.5}$$

$$\boldsymbol{\sigma}_3 = \begin{pmatrix} 1 & 0 \\ 0 & -1 \end{pmatrix} \tag{3.6}$$

$$\boldsymbol{\sigma}^{\pm} = \frac{1}{2}\,\left(\boldsymbol{\sigma}_1 \pm \iota\boldsymbol{\sigma}_2\right) \tag{3.7}$$

In a similar fashion, we establish the isospin matrices and the isospin ladder operators, which share the same numerical values as the Pauli spin matrices.

$$\boldsymbol{\tau}_1 = \begin{pmatrix} 0 & 1 \\ 1 & 0 \end{pmatrix} \tag{3.8}$$

$$\boldsymbol{\tau}_2 = \begin{pmatrix} 0 & -\iota \\ \iota & 0 \end{pmatrix} \tag{3.9}$$

$$\boldsymbol{\tau}_3 = \begin{pmatrix} 1 & 0 \\ 0 & -1 \end{pmatrix} \tag{3.10}$$

$$\boldsymbol{\tau}^{\pm} = \frac{1}{2}\ (\boldsymbol{\tau}_1 \pm \iota\boldsymbol{\tau}_2) \tag{3.11}$$

Allowed Beta-decay There are two distinct types of β-decay processes, categorized based on the spin coupling of the emitted leptons. When the spins of the leptons involved (e^- and ν_e for β^-decay, and e^+ and ν_e for β^+decay) combine to form a total spin of 0, it is referred to as Fermi decay. Conversely, if the spin coupling results in a total spin of 1, this is known as Gamow-Teller (GT) decay. Allowed nuclear β-decays, it is essential to note that the leptons participating in these processes lack any orbital angular momentum. As a result, the transition of a proton to a neutron (or vice versa) can be effectively described through the utilization of isospin ladder operators.

$$\boldsymbol{\tau}^- |n\rangle = |p\rangle \tag{3.12}$$

$$\boldsymbol{\tau}^+ |n\rangle = 0 \tag{3.13}$$

$$\boldsymbol{\tau}^- |p\rangle = 0 \tag{3.14}$$

$$\boldsymbol{\tau}^+ |p\rangle = |n\rangle \tag{3.15}$$

The above expressions are valid because the u and d quarks can be expressed as the following vectors.

$$|u\rangle = \begin{pmatrix} 0 \\ 1 \end{pmatrix} \tag{3.16}$$

$$|d\rangle = \begin{pmatrix} 0 \\ 1 \end{pmatrix} \tag{3.17}$$

Therefore, the operators associated with the two accepted β^-decay processes, namely the Fermi and Gamow-Teller decays, can be represented in the following manner:

$$\sum_{i=1}^{A} \boldsymbol{\tau}^-(i) \equiv \boldsymbol{T}^- \quad (Fermi\ decay) \tag{3.18}$$

$$\sum_{i=1}^{A} \vec{\boldsymbol{\sigma}}(i)\boldsymbol{\tau}^-(i) \equiv \boldsymbol{Y}^- \quad (GT\ decay) \tag{3.19}$$

The equation includes the mass number of the nucleus A, and the summation covers all nucleons. To obtain the operators for β^+decay, simply replace the minus sign to plus in the exponents of $\boldsymbol{\tau}$,$\boldsymbol{T}$, and $\boldsymbol{Y}$ in the Equation 3.18 and 3.19.

To understand how quickly allowed transitions occur, we use a concept called the transition probability, denoted as P_{fi}. It tells us the likelihood of transitioning from an initial state $|i\rangle$ to a final state $|f\rangle$. Calculating this probability involves scattering matrix S_{fi}, a key component in time-dependent perturbation theory. The perturbation series governing the time-evolution operator is subsequently defined as follows [Greiner and Reinhardt, 1996].

$$\hat{U}(t,t_o) = \sum_{n=0}^{\infty} \frac{1}{n!}(-\iota)^n \int_{t_o}^{t} dt_1 \ ... \ \int_{t_o}^{t} dt_n T\left(\hat{H}_1(t_1) \ ... \ \hat{H}_1(t_n)\right) \tag{3.20}$$

$\hat{H}_1$ represents the perturbation component within the system's Hamiltonian. Additionally, we encounter the concept of a time-ordered product denoted as $T\left(\hat{H}1(t_1);...;\hat{H}_1(t_n)\right)$, which encompasses multiple instances of $\hat{H}_1$ occurring at different time. Within this framework, the expression for S_{fi} is derived as follows.

$$S_{fi} = \lim_{t_2\to+\infty} \lim_{t_1\to-\infty} \left\langle f \left| \hat{U}\left(t_2,t_1\right) \right| i \right\rangle \tag{3.21}$$

$$= \sum_n \frac{(-i)^n}{n!} \left\langle f \left| \int_{-\infty}^{+\infty} \mathrm{d}^4x_1 \ \mathrm{d}^4x_2 \cdots \mathrm{d}^4x_n T\left(\hat{\mathcal{H}}\left(x_1\right), \hat{\mathcal{H}}\left(x_2\right), \cdots, \hat{\mathcal{H}}\left(x_n\right)\right) \right| i \right\rangle$$

$$= \delta_{fi} - i \left\langle f \left| \int_{-\infty}^{+\infty} \mathrm{d}^4x \hat{\mathcal{H}}(x) \right| i \right\rangle - \frac{1}{2} \left\langle f \left| \int_{-\infty}^{+\infty} \int_{-\infty}^{+\infty} \mathrm{d}^4x_1 \ \mathrm{d}^4x_2 T\left(\hat{\mathcal{H}}\left(x_1\right), \hat{\mathcal{H}}\left(x_2\right)\right) \right| i \right\rangle + \cdots$$

$|f\rangle$ and $|i\rangle$ correspond to the final and initial states, respectively, while $\hat{\mathcal{H}}$ represents the Hamiltonian density. We introduce the time-dependent state vector as $|\psi(t)\rangle$. The relationship between $|\psi(t)\rangle$ and $|i\rangle$ is outlined as follows.

$$\lim_{t\to-\infty} |\Psi(t)\rangle = |i\rangle \tag{3.22}$$

The transition probability P_{fi} can be written as

$$P_{fi} = S_{fi}^* S_{fi} \tag{3.23}$$

As the principle of four-momentum conservation universally holds for all processes

$$(2\pi)^4\delta^4\left(\sum \mathrm{p}_f - \sum \mathrm{p}_i\right) \equiv (2\pi)^3\delta^3\left(\sum \vec{p}_f - \sum \vec{p}_i\right) 2\pi\delta\left(E_f - E_i\right) \tag{3.24}$$

The expression defines the T matrix using energy-momentum four-vectors denoted as p_f and p_i.

$$S_{fi} = \delta_{fi} + (2\pi)^4\delta^4\left(\sum \mathrm{p}_f - \sum \mathrm{p}_i\right) iT_{fi} \tag{3.25}$$

Upon comparing this equation with the series expansion of the S matrix, specifically in the context of first-order perturbation theory, we obtain

$$
\begin{aligned}
(2\pi)^4\delta^4\left(\sum \mathrm{p}_f - \sum \mathrm{p}_i\right) T_{fi} &= -\left\langle f \left| \int \mathrm{d}^4x\mathcal{H}(x) \right| i \right\rangle \\
&= -(2\pi)^4\delta^4\left(\sum \mathrm{p}_f - \sum \mathrm{p}_i\right) M_{fi}
\end{aligned}
\tag{3.26}
$$

In first-order perturbation theory, it is evident that the matrix element M_{fi} of the Hamiltonian operator in momentum space and T_{fi} primarily differ in their signs. Considering V as the interaction volume and t as the interaction duration, we get

$$
P_{fi} = (2\pi)^4\delta^4\left(\sum \mathrm{p}_f - \sum \mathrm{p}_i\right) Vt\,|T_{fi}|^2 \tag{3.27}
$$

The transition rate per particle in the initial state is given as

$$
\frac{dW_{fi}}{dt} = (2\pi)^4\delta^4\left(\sum \mathrm{p}_f - \sum \mathrm{p}_i\right) |T_{fi}|^2 \tag{3.28}
$$

Integrating over momentum $\vec{p}$ while considering all appropriate final states that adhere to four-momentum conservation, each particle in the final state contributes a phase-space factor $\frac{d^3p}{(2\pi)^3}$. This integration leads to the determination of the decay rate.

$$
\frac{dW}{dt} = (2\pi)^4 \sum_f \int \delta^4\left(\sum \mathrm{p}_f - \sum \mathrm{p}_i\right) \prod_f \frac{d^3p_f}{(2\pi)^3} |T_{fi}|^2 \tag{3.29}
$$

If the matrix element T_{fi} does not depend on kinematics, it can be factored out of the integral, resulting in a simplified form of Equation 3.29.

$$
\frac{dW}{dt} = \rho \cdot |\bar{T}|^2 = \rho \cdot |\bar{M}|^2 \tag{3.30}
$$

In the equation, $\bar{T}$ and $\bar{M}$ represent the spin-averaged matrix elements, while the parameter ρ is defined as

$$
\rho = (2\pi)^4 \sum_{\text{spins}} \int \delta^4\left(\sum \mathrm{p}_f - \mathrm{p}_i\right) \prod_f \frac{d^3p_f}{(2\pi)^3}. \tag{3.31}
$$

In the context of nuclear β-decay, the assumption that the T matrix is not strongly dependent on kinematics holds true [Grotz and Klapdor, 1990], leading to allowed transitions and the subsequent expression:

$$
\begin{aligned}
|\bar{T}|^2 &= G_\beta^2 \left[B_F(f) + B_{GT}(f)\right], \\
\rho &= \frac{1}{(2\pi)^5} \int d^3p_f d^3p_e d^3p_{\bar{\nu}} \delta^3\left(\overrightarrow{p_f} + \overrightarrow{p_e} + \overrightarrow{p_{\bar{\nu}}}\right) \delta\left(E_i - E_f - E_f^{\text{kin}} - E_e - E_{\bar{\nu}}\right),
\end{aligned}
\tag{3.32}
$$

where G_β is the interaction constant, G_β=1.008 $\times$ 10^{-5} m_p^{-2} m_p is the mass of the proton. $\mathrm{B}_F^\pm$ and $\mathrm{B}_{GT}^\pm$ represent the reduced transition probabilities for Fermi decay and Gamow-Teller decay, respectively.

$$
\begin{aligned}
B_F^\pm &= \frac{|\langle N_f||T^\pm||N_i\rangle|^2}{2J_i+1}, \\
B_{GT}^\pm &= \frac{c_A^2\,|\langle N_f||Y^\pm||N_i\rangle|^2}{2J_i+1}.
\end{aligned}
\tag{3.33}
$$

The term c_A represents the renormalization of the weak interaction in Gamow-Teller (GT) decay. If we define the decay energy as Δ_f = E_i - E_f and integrating over $\vec{p}_f$ while disregarding the final kinetic energy E^{kin} of the nucleus nucleus , we can determine the quantity ρ, leading to the following expression

$$\rho = \int d\rho = \frac{1}{(2\pi)^3} \int_{m_e}^{\Delta_f} p_e E_e \left(\Delta_f - E_e\right)^2 dE_e \tag{3.34}$$

$$d\rho = \frac{1}{(2\pi)^3} p_e E_e \left(\Delta_f - E_e\right)^2 dE_e \tag{3.35}$$

Hence, for the total decay rate $\frac{dW_f}{dt}$ to the final state, we obtain the following expression

$$\frac{dW_f}{dt} = \frac{G_\beta^2}{2\pi^3} \left[B_F(f) + B_{GT}(f)\right] \int_{m_e}^{\Delta_f} p_e E_e \left(\Delta_f - E_e\right)^2 dE_e \tag{3.36}$$

or

$$\frac{dW_f}{dt dE_e} = \frac{G_\beta^2}{2\pi^3} p_e E_e \left(\Delta_f - E_e\right)^2 \left[B_F(f) + B_{GT}(f)\right]. \tag{3.37}$$

To account for the Coulomb interaction between nuclei and electrons, a correction factor is introduced to refine the calculations, as follows

$$F\left(Z, E_e\right) = \left|\psi(0)_{\text{with}} / \psi(0)_{\text{without}}\right|^2 \tag{3.38}$$

The correction factor, known as the Fermi function F(Z, E), takes into account the Coulomb interaction between electrons and nuclei. It is determined by comparing the electron wave function $\psi(0)_{\text{with}}$, which considers Coulomb interaction for an extended nucleus, to $\psi(0)_{\text{without}}$, which neglects Coulomb interaction. For non-relativistic electrons influenced by a point-like nucleus, this correction factor can be expressed analytically.

$$F_{NR}(Z, E) = \frac{2\pi\eta}{1 - e^{-2\pi\eta}} \tag{3.39}$$

where

$$\eta = \pm \frac{Ze^2}{v_e} \quad \text{for } \beta^{\mp}\text{decay} \tag{3.40}$$

v_e represents the velocity of the emitted electron/positron as it moves towards infinity. In the case of heavy nuclei with a large atomic number (Z), the calculation of F(Z, E) necessitates solving the relativistic Dirac equation, considering the Coulomb potential for an extended nucleus. This modification also affects dρ, leading to the following expression

$$d\rho = \frac{1}{2\pi^3} F(Z, E) \left(\Delta_f - E_e\right)^2 p_e E_e dE_e. \tag{3.41}$$

Thus, we arrive at the expression for the decay rate of allowed transitions per electron-energy interval as follows

$$\frac{dW}{dt dE_e} = \frac{G_\beta^2}{2\pi^3} F(Z, E) p_e E_e \left(\Delta_f - E_e\right)^2 \left[B_F + B_{GT}\right] \tag{3.42}$$

By integrating over the electron energy

$$\frac{dW}{dt} = \int_{m_E}^{\Delta_f} \frac{dW}{dt dE_e} dE_e = \frac{G_\beta^2 m_e^5}{2\pi^3} f \left[B_F + B_{GT}\right], \tag{3.43}$$

$$f \equiv \frac{1}{m_e^5} \int_{m_e}^{\Delta_f} F(Z,E) p_e E_e \left(\Delta_f - E_e\right)^2 dE_e. \tag{3.44}$$

The Fermi integral, denoted as "f´´ is available in tabulated form according to [Gove and Martin, 1971]. The relationship between the decay rate and the partial half-life $t_{1/2}$ can be summarized as follows

$$t_{1/2} = [dW/dt]^{-1} \ln 2 \tag{3.45}$$

we have

$$f t_{1/2} = \frac{2\pi^3 \ln 2}{G_\beta^2 m_e^5} \frac{1}{[B_F + B_{GT}]} \equiv \frac{4\pi D}{[B_F + B_{GT}]} \tag{3.46}$$

Equation 3.46 introduces the concept of the *(ft)* value, where $t_{1/2}$ signifies the partial half-life linked to a transition towards a specific energy level E_f within the daughter nucleus. To calculate the overall half-life $T_{1/2}$ for allowed β-decay into the daughter nucleus, a summation across all final states E_f engaged in the β-decay event is required

$$T_{1/2}^{-1} = \sum f_f \frac{B_F\left(E_f\right) + B_{GT}\left(E_f\right)}{4\pi D} \tag{3.47}$$

3.3.1 Forbidden Transition

In the decay of extended objects like atomic nuclei, certain transitions involve leptons carrying orbital angular momentum, known as "forbidden" transitions. This term indicates that transitions involving the transfer of orbital angular momentum have significantly reduced decay rates. This reduction in decay rate arises from the fact that transitions with lepton orbital angular momentum (l) are associated with higher-order terms in a multipole expansion of the lepton wave function, where the expansion parameter is R_q. Here, R represents the radius of the nucleus, and q represents the momentum exchanged between the nucleus and the leptons [Grotz and Klapdor, 1990]. In the case of unique forbidden transitions, where only a single multipole component and a single transition operator are involved, there exists a direct relationship between the quantity $f_n t_{1/2}$ and the reduced transition strength denoted as B_n.

$$f_n t_{1/2} = \frac{2\pi^3 \ln 2}{G_\beta^2 m_e^5 B_n} \tag{3.48}$$

Table 3.1: *Selection rules for the allowed and forbidden β-decays [Grotz and Klapdor, 1990].*

Type	**L**	**Δ J (for F)**	**Δ J (for GT)**	**Δ π**
Allowed	0	0	(0), 1	No
First Forbidden	1	(0), 1	0, 1, 2	Yes
Second Forbidden	2	(1), 2	2, 3	No
Third Forbidden	3	(2), 3	3, 4	Yes

The determination of whether a β decay is allowed or forbidden can be made by comparing the log(ft) value with reference figures. Specifically, Fig. 3.4 is used for allowed, while Fig. 3.5 is used for the type of forbidden decays. By comparing the calculated log(ft) value with the values in these figures, one can classify the β decay as either allowed or forbidden [Turkat et al., 2023].

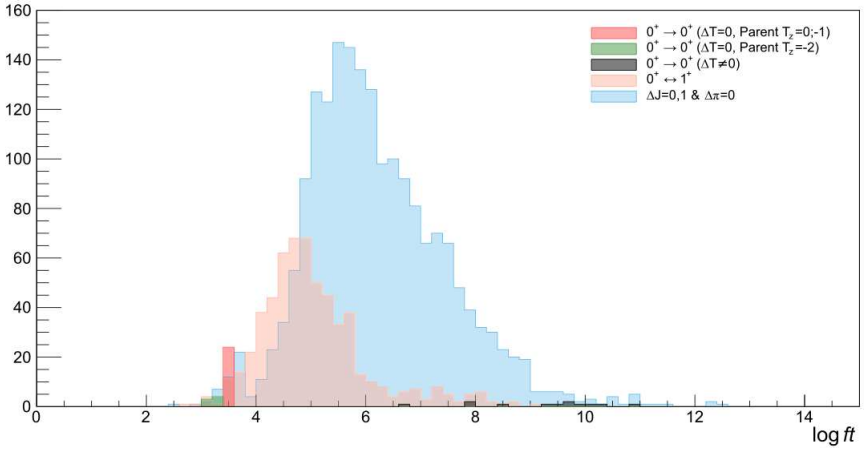

Figure 3.4: *Transitions classified as allowed, are highlighted in shades of pink and light blue. Various shades may emerge as a result of color overlap. Additionally, isospin-forbidden transitions are shown in black, providing a clear differentiation within the display. [Turkat et al., 2023].*

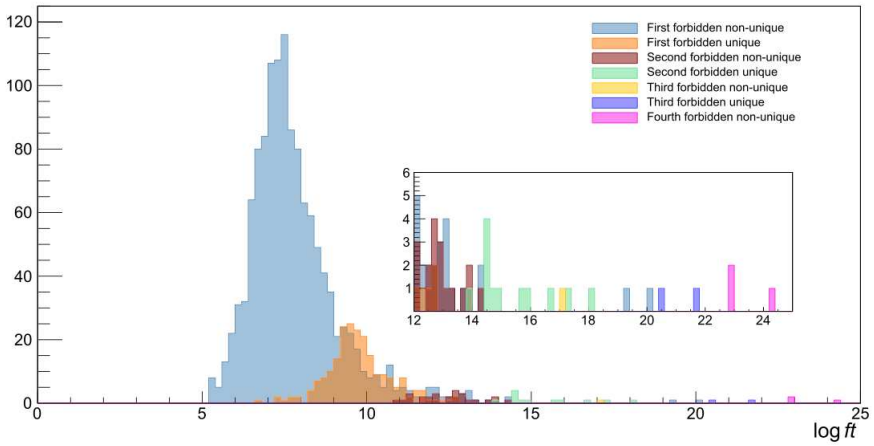

Figure 3.5: *The log(ft) values for the different types of forbidden decay. [Turkat et al., 2023].*

3.4 Nuclear Shell Model

The nuclear shell model serves as a fundamental approach for comprehending the behavior of individual particles within atomic nuclei. This overview encompasses different models, commencing with the elementary spherical shell model and evolving towards more sophisticated models that incorporate nuclear deformation and collective motion.

3.4.1 Spherical Shell Model

In the nuclear shell model, it is assumed that each nucleon interacts with a central potential created by all other nucleons in the nucleus. The model begins by exploring two fundamental potentials: the infinite square well and the harmonic oscillator potential [Krane, 1991]. The primary objective is to find solutions to the three-dimensional time-independent Schrodinger Equation for each of these scenarios.

$$\frac{-\hbar^2}{2m}\left(\frac{\partial^2\psi}{\partial x^2}+\frac{\partial^2\psi}{\partial y^2}+\frac{\partial^2\psi}{\partial z^2}\right)+V(x,y,z)\psi(x,y,z)=E\psi(x,y,z) \tag{3.49}$$

where ψ is a wavefunction, V(x, y, z) is the potential of the system, m is the mass of the particle, and E is the energy of the system.
For the three-dimensional square well, the length (at x, y, and z) is defined as "a". Then we can write

$$\frac{-\hbar^2}{2m}\left(\frac{\partial^2\psi}{\partial x^2}+\frac{\partial^2\psi}{\partial y^2}+\frac{\partial^2\psi}{\partial z^2}\right)=E\psi(x,y,z) \tag{3.50}$$

and the corresponding energy is given by

$$E_{n_x,n_y,n_z}=\frac{\hbar^2\pi^2}{2ma^2}\left(n_x^2+n_y^2+n_z^2\right) \tag{3.51}$$

where n_x, n_y, and n_z are integers. Some of the calculated values (along with their degeneracy) are presented in Table 3.2.

In the case of the harmonic oscillator potential, the problem is formulated within the framework of spherical coordinates, and the harmonic oscillator potential associated with this setup is represented as follows.

$$V(r)=\frac{1}{2}kr^2 \tag{3.52}$$

k is the oscillator constant and r is the radial distance measured from the equilibrium position. The equation of energy is given as

$$E_n=\hbar\omega_o\left(n+\frac{3}{2}\right) \tag{3.53}$$

where n is the number of the oscillator shell. The shell closure numbers, as illustrated in Fig. 3.6, do not coincide for atomic numbers exceeding 20 when considered under both potentials. Furthermore, neither potential accurately predicts the experimentally observed shell closure numbers, which are 2, 8, 20, 28, 50, 82, 126, and 184 [Mayer, 1949].

Table 3.2: *Combination of n_x, n_y, and n_z and degeneracy.*

$\mathbf{E}_{n_x,n_y,n_z}$	n_x	n_y	n_z	n^2	g
E_{111}	1	1	1	3	1
E_{112}	1	1	2	6	
E_{121}	1	2	1	6	3
E_{211}	2	1	1	6	
E_{122}	1	2	2	9	
E_{212}	2	1	2	9	3
E_{211}	2	1	1	9	
E_{112}	1	1	3	11	
E_{131}	1	3	1	11	3
E_{311}	3	1	1	11	
E_{222}	2	2	2	12	1

The Woods-Saxon Potential is the preferred model for describing the nuclear potential due to its better alignment with the nucleon density distribution, providing a more precise description. The potential is given as

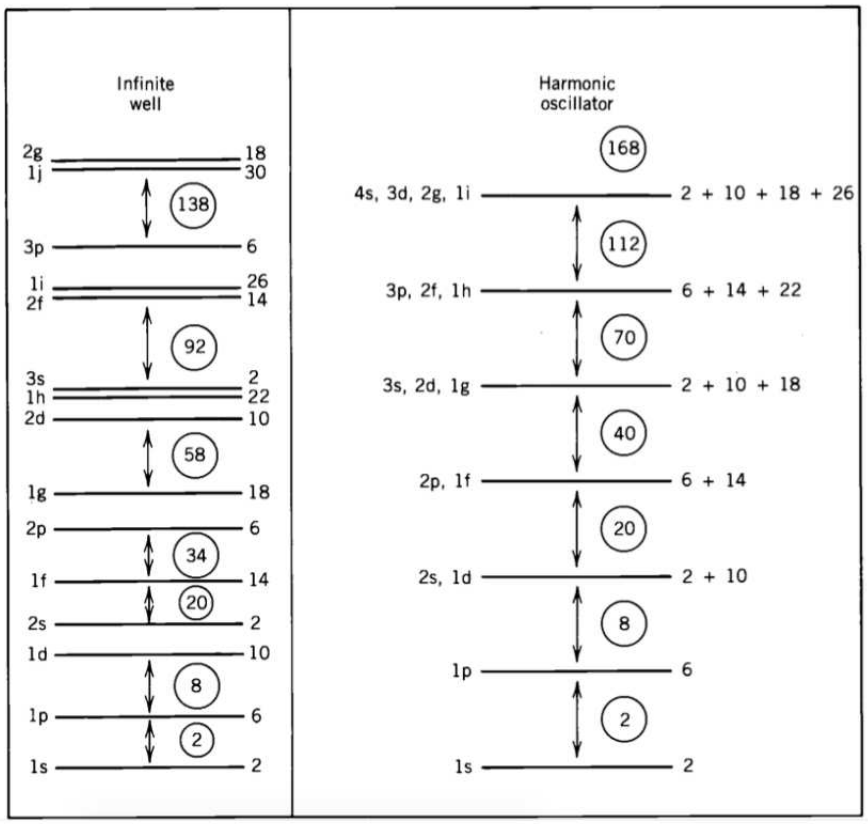

Figure 3.6: *The figure illustrates energy levels obtained from solving the Schrödinger equation for two different potential scenarios: the 3D infinite well and the harmonic oscillator. The numbers enclosed in circles represent the nucleon associated with specific shell closure [Krane, 1991].*

$$V(r) = \frac{V_o}{1 + e^{\frac{r - R_o A^{1/3}}{a}}} \tag{3.54}$$

where A is the number of nucleons, $V_o \approx$ -50 MeV, $R_o \approx$ 1.2fm, and a $\approx$ 0.524 fm [Krane, 1991]. In Fig. 3.7, the Woods-Saxon potential is superimposed on the square well and harmonic oscillator potentials, highlighting its compatibility with these models.

However, it is evident that the Woods-Saxon potential alone fails to accurately reproduce the established magic numbers To address this, a spin-orbit term $V_{so}(r)\ \vec{l} \cdot \vec{s}$ is added to Equation 3.54 This modification significantly improves the agreement between theoretical predictions and experimental shell closure numbers shown in Fig. 3.8. Energy levels within a spherical nucleus exhibit a degeneracy of $2j + 1$ due to spherical symmetry. The total angular momentum j of a state results from the sum of its spin (s) and orbital angular momentum (l), expressed as $j = l + s$ [Krane, 1991, Mayer, 1949].

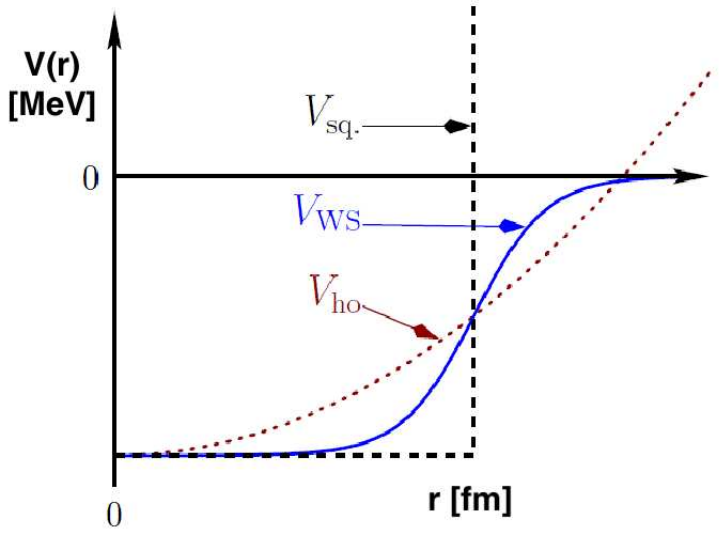

Figure 3.7: *Comparison of the Woods-Saxon Potential with the square well and harmonic oscillator potentials [Anwer Ahmed, 2015]*

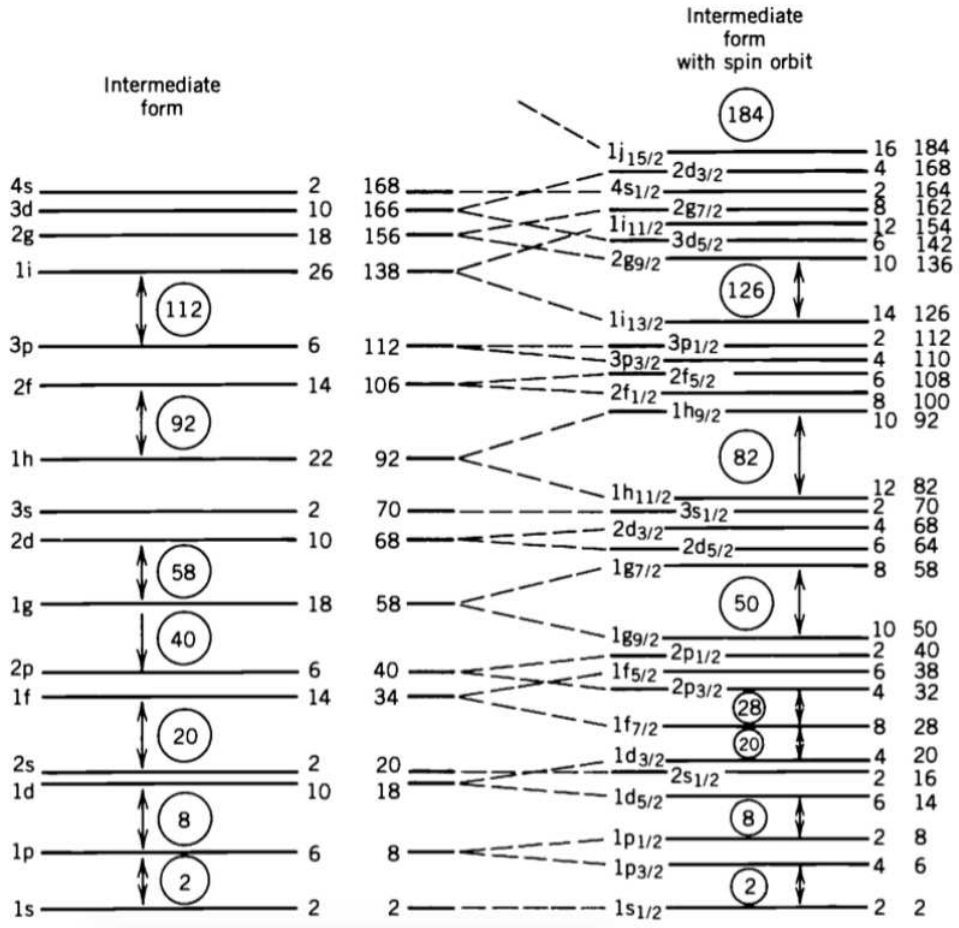

Figure 3.8: *The addition of a spin-orbit term to the Woods-Saxon Potential successfully reproduces the magic numbers in the energy levels of nuclei [Krane, 1991].*

3.5 Gamma Decay

After undergoing β-decay, the resultant daughter nucleus frequently exists in an excited state rather than its ground state. During the de-excitation process to reach the ground state, this excited nucleus emits high-energy photons called γ-rays. This de-excitation process often involves the emission of multiple subsequent γ-rays in a cascade. The energy of these emitted γ-rays can vary, spanning from less than 100 keV to over 10 MeV [Krane, 1991].
γ-decay differs from β-decay because it does not alter the number of protons and neutrons in the nucleus. Instead, it changes the energy of the nucleus. The energy of the emitted γ-ray (E_γ) is determined by subtracting the energy of the final state (E_f) from the energy of the initial state (E_i). By carefully studying the γ-rays emitted by a nucleus, we can gather information about its excited-state structure [Krane, 1991].

γ decay :

$$ {}^{A}_{Z}X^{*}_{N} \longrightarrow {}^{A}_{Z}X_{N} + \gamma $$

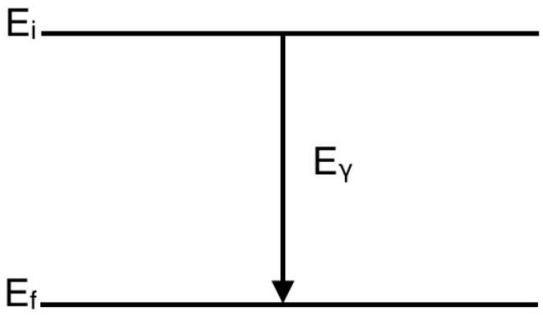

Figure 3.9: *The energy of the emitted γ-ray, denoted as E_γ, is determined by the difference between the energy of the initial state (E_i) and the energy of the final state (E_f).*

In classical electromagnetism, the radiated power from an electric or magnetic multipole exhibits a particular mathematical form.

$$ P(\sigma L) = \frac{2(L+1)}{\epsilon_o L[(2L+1)!!]^2} \left(\frac{\omega}{c}\right)^{2L+2} [m(\sigma L)^2] \tag{3.55} $$

The expression involves σ representing either electric (E) or magnetic (M) radiation, m(σL) denoting the time-dependent amplitude of the electric or magnetic moment, P(σL) represents the power radiated, and the double factorial representing a factorial calculation over odd terms only [Krane, 1991]. The angular momentum term L specifies the multipole order, with L = 1 corresponding to a dipole, L = 2 to a quadrupole, and higher-order terms following a similar pattern.

In quantum mechanics, the multipole moment m(σL) is replaced by the multipole operator σL, responsible for transitioning the nucleus from an initial state ψ_i to a final state ψ_f. Similar to β-decay, the matrix element m_{fi} plays a crucial role in determining the transition probability between these initial and final states.

$$ m_{fi}(\sigma L) = \langle \psi_f | \sigma L | \psi_i \rangle \tag{3.56} $$

By substituting the multipole operator from Equation 3.56 and considering the photon energy as $\hbar\omega$, the decay constant associated with photon emission can be represented in relation to the radiated power $P(\sigma L)$ as described in Equation 3.55

$$\lambda(\sigma L) = \frac{P(\sigma L)}{\hbar\omega} = \frac{2(L+1)}{\epsilon_o \hbar L[(2L+1)!!]^2} \left(\frac{E_\gamma}{\hbar c}\right)^{2L+1} \quad B(\sigma L; I_i \rightarrow I_f) \tag{3.57}$$

3.5.1 Transition rates

The relationship between the matrix element and the reduced transition rate is given as

$$B(\sigma L; I_i \rightarrow I_f) = \frac{|\langle \psi_f || \sigma L || \psi_i \rangle|^2}{2I_i + 1} \tag{3.58}$$

where $|\langle \psi_f || \sigma L || \psi_i \rangle|^2$ is the reduced matrix element. Before extracting further information from Equation 3.58, it is necessary to evaluate the matrix element. Assuming that γ-ray emission results from the transition of a single particle between two shell-model orbitals, the transition probability for an electric transition EL is defined as follows

$$\lambda^W(EL) \cong \frac{8\pi(L+1)}{L[(2L+1)!!]^2} \frac{e^2}{4\pi\epsilon_o\hbar c} \left(\frac{E_\gamma}{\hbar c}\right)^{2L+1} \left(\frac{3}{L+3}\right)^2 cR^{2L} \tag{3.59}$$

and for a magnetic transition

$$\lambda^W(ML) \cong \frac{8\pi(L+1)}{L[(2L+1)!!]^2} \frac{e^2}{4\pi\epsilon_o\hbar c} \left(\frac{E_\gamma}{\hbar c}\right)^{2L+1} \left(\frac{3}{L+3}\right)^2 \left(\mu_p - \frac{1}{L+1}\right)^2 \left(\frac{\hbar}{m_p c}\right)^2 cR^{2L-2} \tag{3.60}$$

The expressions in Equations. 3.59 and 3.60 are derived based on certain approximations, including the use of the nuclear radius $R \approx R_0\ A^{(1/3)}$, where R_0 is approximately 1.2 fm, and E is the energy [Krane, 1991].

Reduced transition rates, $B(\sigma L)$, for single-particle transitions can be estimated using traditional expressions like those summarized below:

$$B^W(EL) = \frac{1}{4\pi} \left(\frac{3}{L+3}\right)^2 e^2\ R^{2L} \tag{3.61}$$

$$B^W(ML) = \frac{10}{\pi} \left(\frac{3}{L+3}\right)^2 \mu_N^2\ R^{2(L-1)} \tag{3.62}$$

The estimates provided in Equations 3.61 and 3.62 can be seen as the substituted factors for $|\langle \psi_f | \sigma L | \psi_i \rangle|^2$ in comparison to Equation 3.56, with some additional minor factors included [Krane, 1991, Brown, 2005, Siegbahn and Axel, 1966].

The Weisskopf estimates, which provide rough approximations for single-particle transition rates within a nucleus, are useful tools for gaining insight into nuclear transitions. These estimates, while not dependent on the wave functions of the initial and final states, can offer valuable information about the transition process. In cases where experimental decay rates are significantly larger than the Weisskopf estimate, it may indicate that more than one nucleon is involved in the decay process.
To calculate energy- and nucleus-dependent Weisskopf estimates [Krane, 1991], one can set the term $[\mu_p - 1/L + 1]^2 = 10$ in Equation 3.60. This allows for the evaluation of Equation 3.59 and 3.60 at various angular momenta L. Selected lower-order electric and magnetic Weisskopf estimates are presented in Table 3.3.

Table 3.3: *Weisskopf provides estimates for various electric and magnetic transitions. These estimates are related to the energy E of the emitted γ-ray (measured in MeV) and the number of nucleons denoted as A.*

σL	$B^W[e^2fm^{2L}]$	$\lambda^W s^{-1}$
E1	6.5×10^{-2} $A^{2/3}$	1.0×10^{14} $A^{2/3}$ E^3
E2	5.94×10^{-2} $A^{2/3}$	7.3×10^{7} $A^{4/3}$ E^5
E3	5.94×10^{-2} $A^{2/3}$	34 A^2 E^7
E4	6.29×10^{-2} $A^{2/3}$	1.1×10^{-5} $A^{8/3}$ E^9
M1	1.79	5.6×10^{13} E^3
M2	1.65 $A^{2/3}$	3.5×10^{7} $A^{2/3}$ E^5
M3	1.65 $A^{2/3}$	16 $A^{4/3}$ E^7
M4	1.75 $A^{2/3}$	4.5×10^{-6} A^2 E^9

3.5.2 Selection Rules of γ Transition

In γ-ray transitions, the conservation of angular momentum is a fundamental principle. It relates the initial angular momentum (I_i), final angular momentum (I_f), and the angular momentum of the emitted γ-ray (L_γ) through the following equation [Krane, 1991].

$$I_i = I_f + I_\gamma \tag{3.63}$$

The possible values of L_γ are determined by combining the angular momenta of three vectors

$$|I_i - I_f| \leq L_\gamma \leq (I_i - I_f) \tag{3.64}$$

Given that γ-ray transitions are fundamentally electromagnetic, they are subject to the constraint of conserving parity, given as

$$\pi(EL) = (-1)^L \tag{3.65}$$

$$\pi(ML) = (-1)^{L+1} \tag{3.66}$$

The selection rules for γ-decay are determined by the interplay of angular momentum coupling and parity considerations. Specifically, the parity of electric and magnetic transitions is opposite for a given angular momentum. Consequently, the nature of γ-rays is frequently categorized based on the lowest order multipole of their emission. Table 3.4 provides common designations for transitions characterized by low angular momentum.

Table 3.4: *Electric and Magnetic multipoles and their associated angular momentum (l) and the parities (π).*

Multipolirity	l	π	Multipolirity	l	π
M1	1	+	E1	1	-
M2	2	-	E2	2	+
M3	3	+	E3	3	-
M4	4	-	E4	4	+
M5	5	+	E5	5	-

3.6 Gamma Ray Interaction with Matter

The interaction of γ-rays with a material is crucial for understanding background signals in a detector. γ-rays can interact with matter through three main processes, and the dominance of each process depends on the energy of the photon [Knoll, 2010]. These processes are Photoelectric Absorption, Compton Scattering, and Pair Production. The energy ranges over which these processes are most prevalent are illustrated in Fig. 3.10.

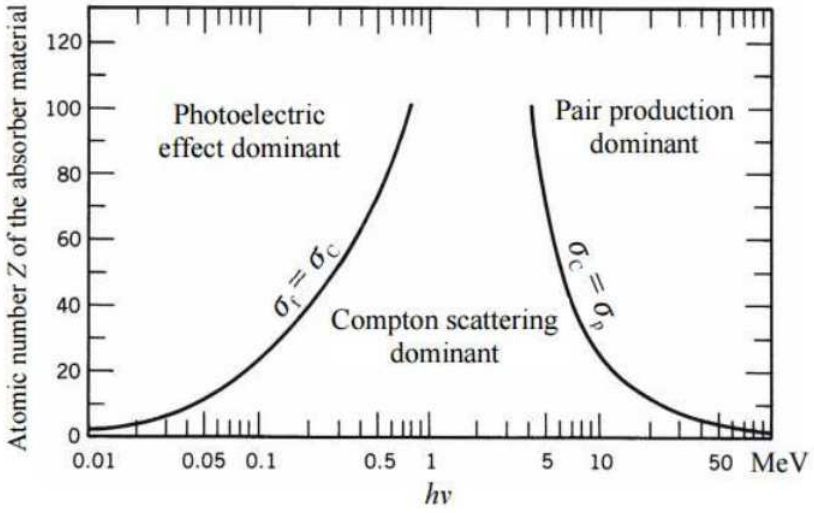

Figure 3.10: *The interactions of γ-rays with matter involve three main processes, each dominant in specific energy ranges. [Knoll, 2010]*

3.6.1 Photoelectric Absorption

In photoelectric absorption, a photon collides with an electron within a material, transferring all of its energy to the electron, and ceases to exist. As a result, an energetic electron known as a photoelectron is expelled from one of the atom's bound electron shells. It is important to note that this interaction occurs with the atom as a whole and cannot happen with free electrons. The energy of the photoelectron, denoted as E_o, is determined by the equation $E_o = E_\gamma$ - E_b, where E_γ represents the initial energy of the photon, and E_b represents the binding energy of the electron shell involved [Knoll, 2010].

When a photon's interaction with an electron in a material leads to the expulsion of the electron (photoelectron), it creates a temporary vacancy in one of the atom's electron shells. This vacancy is promptly filled either by capturing free electrons from the surrounding medium or by redistributing electrons from other shells within the same atom. This filling process emits characteristic X-rays. These X-rays can either be absorbed within the material through photoelectric absorption or escape from it.

In some instances, the initial vacancy in the inner shell may be occupied by a second atomic electron from a higher shell. This process necessitates the simultaneous loss of energy. Consequently, a third electron, known as an Auger electron, is emitted, carrying away the excess energy. This transition occurs through a radiationless process [Bryan, 2023]. A rough estimate to describe the probability of photoelectric absorption is given as

$$\tau \propto \frac{Z^n}{E_\gamma^3} \tag{3.67}$$

n falls within the range of 4 to 5 [Knoll, 2010]. The strong dependence of photoelectric absorption on the atomic number (Z) is the main factor driving the widespread use of high-Z materials in gamma-ray spectroscopy detectors.

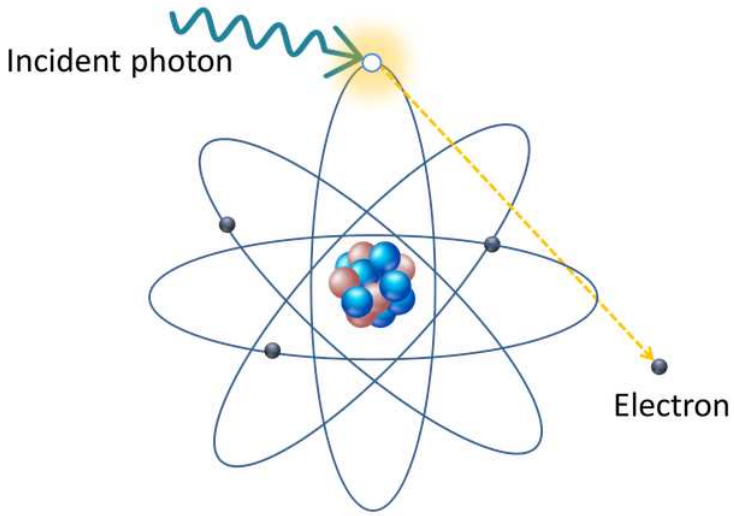

Figure 3.11: *Photo-electric Effect [int,].*

3.6.2 Compton Scattering

Compton scattering involves a gamma ray interacting with a free or loosely bound electron, resulting in a partial energy transfer from the γ-ray to the electron. This interaction conserves both momentum and energy.

$$E_\gamma = E_{sc} + E_{ce} + E_b \tag{3.68}$$

E_{sc} is the energy of the scattered photon, E_{ce} is the energy of the ejected electron, and E_b is the binding energy of the electron [Bryan, 2023]. In Compton scattering, the photon interacts with outer-shell (valence) electrons, and because the binding energy of outer-shell electrons is very small, it leads to partial energy transfer during the interaction, we can write

$$E_\gamma \approx E_{sc} + E_{ce} \tag{3.69}$$

The energy of the scattered photon, denoted as E_{sc}, in relation to the scattering angle (θ) and the energy of the original photon (E_γ) can be expressed as:

$$E_{sc} = \frac{E_\gamma}{1 + \frac{E_\gamma}{m_o c^2}(1 - cos(\theta))} \tag{3.70}$$

In Compton scattering, as the scattering angle (θ) increases, the energy of the scattered photon (E_{sc}) decreases. This phenomenon is described by the equation in which $m_o c^2$ represents the rest energy of the electron. Compton scattering is the primary interaction for gamma rays with intermediate energy levels, typically ranging from 1 to 3 MeV [Knoll, 2010, Bryan, 2023].

3.6.3 Pair Production

In the process of pair production, a gamma ray interacts with the nucleus of an absorbing material, leading to the creation of an electron and a positron, collectively referred to as a "pair". As a consequence of pair production, the gamma-ray is entirely absorbed and ceases to exist [Knoll, 2010]. Pair production is a phenomenon that can occur when a gamma ray has an energy greater than or equal to twice the rest mass of an electron, which is approximately 1.022 MeV. In pair production, the gamma-ray transforms its energy into the creation of an electron and a positron, both with kinetic energy, while the gamma-ray itself ceases to exist [Knoll, 2010].

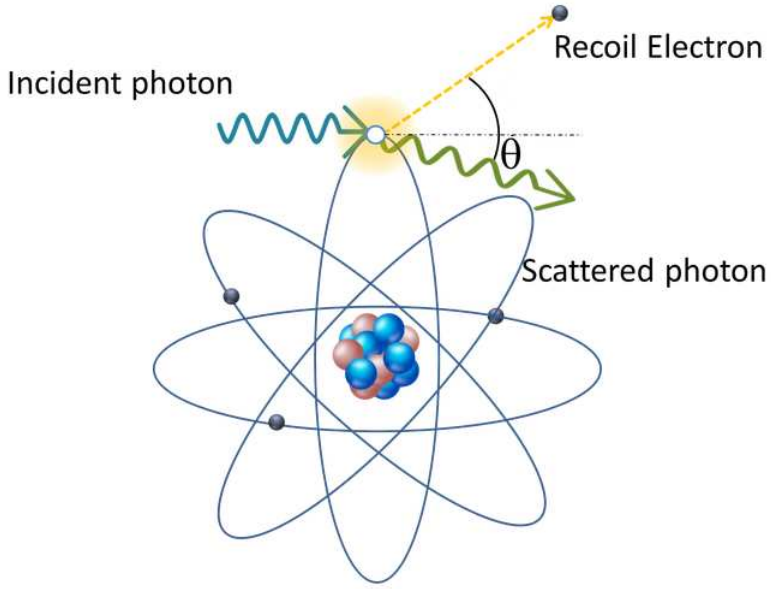

Figure 3.12: *Compton Effect [int,].*

$$E_\gamma = E_{\beta+} + E_{\beta-} + 1.022 \text{ MeV} \tag{3.71}$$

In pair production, when a gamma ray interacts and creates an electron and a positron, these particles may have excess kinetic energy. They lose this excess energy through interactions with nearby matter, such as ionization and excitation processes. The positron eventually annihilates. The two resulting 0.511 MeV photons from this annihilation can have different fates within a gamma-ray detector. They may both escape the detector, be absorbed in the detector, or one photon can escape while the other gets absorbed. The probability of pair production is not easily described by a simple mathematical expression, but it generally increases with the square of the atomic number of the absorbing material [Knoll, 2010].

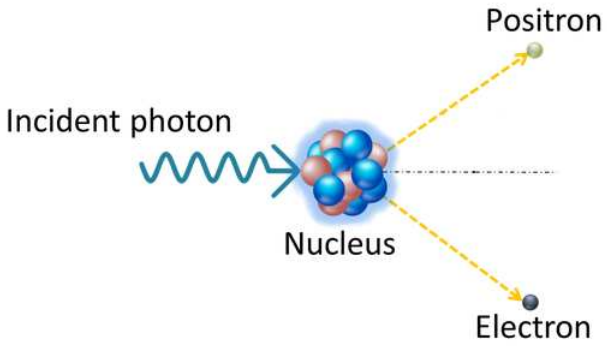

Figure 3.13: *Pair Production [int,].*

3.6.4 Gamma-Ray Interaction and Detection

Gamma-ray spectroscopy involves using detectors to capture both the intensity and energy information of gamma rays. The resulting plot of energy versus the number of counts is called the energy spectrum. This spectrum can help identify different radionuclides within a sample because each radionuclide has a unique gamma-ray spectrum, and the total spectrum is a combination of individual radionuclide decays. To interpret a gamma-ray spectrum accurately, it is crucial to understand the various features of the spectrum, which can be explained by considering how gamma rays interact with matter. Fig. 3.14 illustrates the three main types of interactions that gamma rays can experience within a detector

and the relative significance of these interactions for different absorber materials across a range of gamma-ray energies. In most detectors, characteristic X-rays and Auger electrons generated during gamma-ray interactions are confined within the detector due to its size. Consequently, the entire energy of the gamma-ray is absorbed by the detector, leading to the formation of a distinct and well-defined full-energy peak in the energy spectrum [Knoll, 2010]. When the incident gamma-ray energy is less than 1.022 MeV, the resulting spectrum primarily comprises two components:

- **Compton Continuum:** This represents a continuous range of energies resulting from Compton scattering interactions.
- **Full Energy Peak:** This is a narrow peak in the spectrum, corresponding to the photoelectric absorption of the incident gamma ray.

These components can be observed in the energy spectrum, as shown in Fig. 3.15(left).

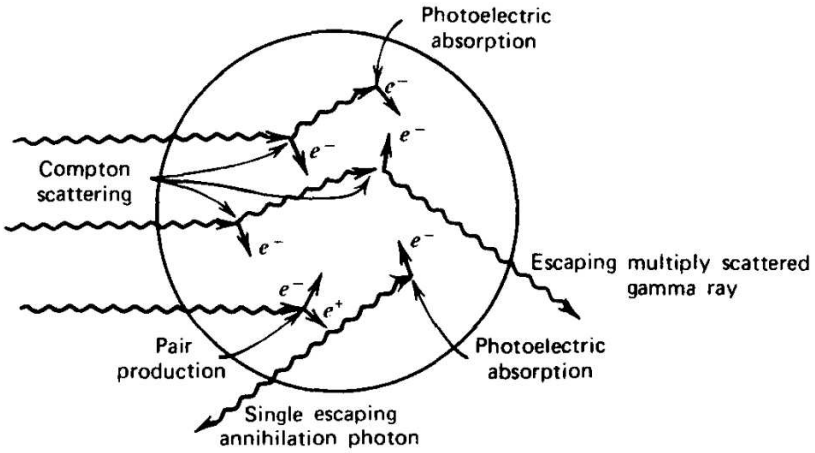

Figure 3.14: *The three major interactions that play a crucial role in gamma-ray spectroscopy and are important for understanding how gamma rays interact with materials [Knoll, 2010].*

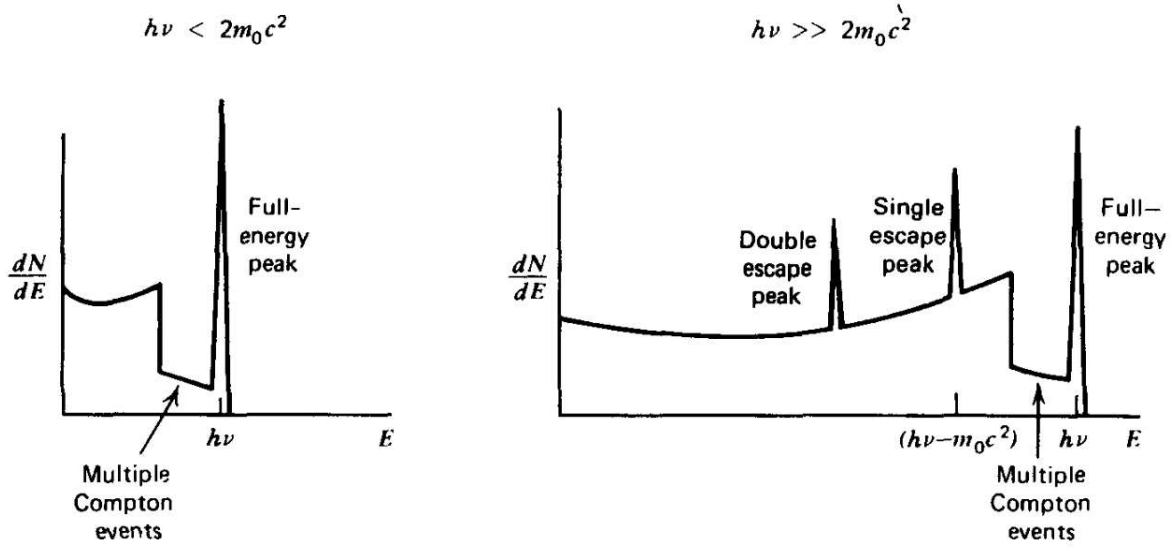

Figure 3.15: *Response of the detector at $E<2m_oc^2$ (left) and at $E>>2m_oc^2$ (right) [Knoll, 2010].*

When the energy of an incident gamma ray is equal to or greater than 1.022 MeV, pair production can occur within the detector. In this process:

- **Single Escape Peak:** If one of the resulting 0.511 MeV photons manages to escape the detector, it generates a peak in the energy spectrum that is positioned 0.511 MeV below the primary photopeak.
- **Double Escape Peak:** If both 0.511 MeV photons escape the detector, it leads to a peak in the energy spectrum positioned at 1.022 MeV below the primary photopeak.

These additional peaks provide valuable information in gamma-ray spectroscopy and help identify the occurrence of pair production events within the detector, See Fig. 3.15 (right).

Chapter 4
Experimental Facility

4.1 TRIUMF

TRIUMF serves as Canada's premier facility for accelerator-based Nuclear and Particle Physics, Fig. 4.1. Its key feature is the world's largest cyclotron, capable of accelerating negative hydrogen ions to energies reaching up to 520 MeV. The process involves stripping protons of their two electrons using a carbon wire or foil to reverse their charge, after which they are directed into one of four beamlines through magnetic manipulation. This versatile facility enables proton extraction at various energy levels, ranging from 65 to 520 MeV [Blackmore, 2000].

TRIUMF's multiple beam lines are essential for a wide range of experiments, spanning medical imaging and materials science. A notable application involves providing protons to the Isotope Separator and Accelerator (ISAC). Protons are directed onto a target, like Uranium-Carbide (UC_x), to generate rare isotope beams through processes like spallation, fission, and fragmentation. These desired isotopes are then extracted using the Isotope Separator On-Line (ISOL) technique and supplied to various experiments within the ISAC facility. In ISAC-I, low-energy ions are transported via Low-Energy Beam Transport (LEBT), while ISAC-II accelerates ions to energies ranging from 1.5 to 15 MeV/u for experiments such as TIGRESS [Dilling et al., 2014].

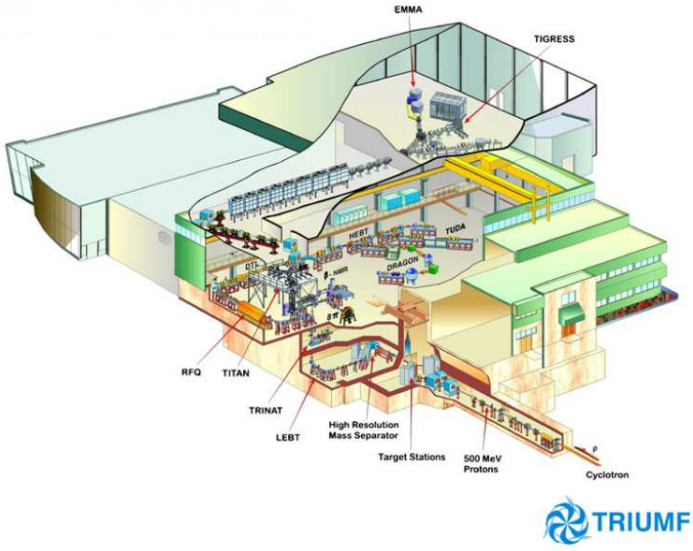

Figure 4.1: *TRIUMF-ISAC Facility [Dilling et al., 2014].*

4.1.1 GRIFFIN

GRIFFIN is an advanced and highly efficient gamma-ray spectrometer designed for conducting decay spectroscopy experiments, see Fig. 4.2. It is specifically tailored for use with low-energy radioactive ion beams sourced from TRIUMF's ISAC-I radioactive ion beam facility. GRIFFIN consists of sixteen high-purity germanium (HPGe) gamma-ray detectors designed in a clover-type configuration and

within each clover, there are 4 crystals, resulting in a combined total of 64 crystals, Fig. 4.3. These detectors are equipped with custom digital signal processing electronics and are complemented by various auxiliary detection systems for research purposes [Svensson and Garnsworthy, 2014].

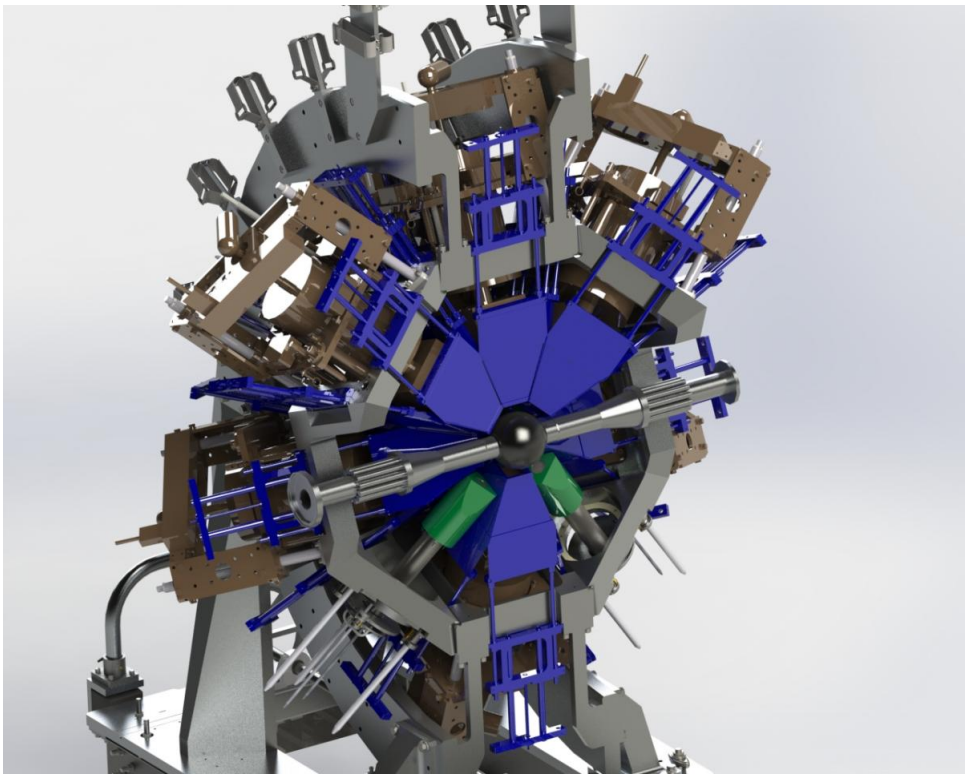

Figure 4.2: *Germanium detectors are shown in brown and are enclosed by BGO detectors represented in purple. $LaBr_3$ detectors are represented in green. [ged,].*

4.1.2 High Purity Germanium

Gamma-ray spectroscopy is a technique used to analyze complex gamma-ray spectra resulting from radioactive decay. These spectra contain valuable information about isotope properties, but the presence of multiple peaks makes it crucial to achieve high resolution. Germanium (Ge) crystals are excellent for this purpose, offering superior energy resolution for gamma rays, enabling the identification of individual peaks, and providing insights into isotope characteristics [ged,].

Germanium, a semiconductor material, is used in gamma-ray spectroscopy detectors. These detectors feature two electrical contacts with a high-voltage electrical field (typically between 3500 and 4000 V) applied incrementally to prevent crystal damage. This field operates within a designated area referred to as the depletion region. Gamma-ray detectors using Germanium operate by allowing γ-rays to interact within the Germanium crystal. When this interaction occurs, electrons are released from the Germanium atoms. These freed electrons move toward the electrical contacts, creating an electric current. The collected charge on the contacts is directly proportional to the original γ-ray energy, enabling the determination and display of the γ-ray's energy on a spectrum [Khandaker, 2011].

GRIFFIN is constructed with 16 high-purity Germanium (HPGe) clover detectors arranged in a close-packed array. The GRIFFIN structure has a rhombicuboctahedral shape, with 16 of its 18 faces covered by the HPGe detectors. The remaining two faces are dedicated to servicing the beamline and tape system [Garnsworthy et al., 2019]. The GRIFFIN HPGe detectors are designed as four germanium crystals closely packed in a clover arrangement. These crystals have dimensions of 60 mm in diameter and 90 mm in length, with a taper of 22.5 degrees over the first 30 mm of their outer edges to facilitate close-packing. To ensure optimal performance, the crystals are reverse-biased to extend the depletion region throughout the crystal volume. Additionally, they are cooled using liquid

nitrogen through a single cryostat [Rizwan et al., 2016].

The GRIFFIN HPGe detectors are favored for γ-ray spectroscopy due to their remarkable energy resolution. Initially commissioned with 64 HPGe crystals, they exhibited energy resolutions of better than $\sigma = 0.54$ keV and $\sigma = 0.86$ keV for 122.0 keV and 1332.5 keV source peaks, respectively. Additionally, each crystal had a relative efficiency of 37.9% or higher at a 25 cm distance from the source, relative to a 3" $\times$ 3" NaI scintillator. On average, across all 64 crystals, the energy resolution for the 1332.5 keV source peak was $\sigma = 0.80(3)$ keV, and the efficiency was 41(1)%. Furthermore, the timing resolution for all GRIFFIN HPGe crystals exceeded 10 ns for detected γ-rays above 100 keV. More details can be found in Reference [Rizwan et al., 2016].

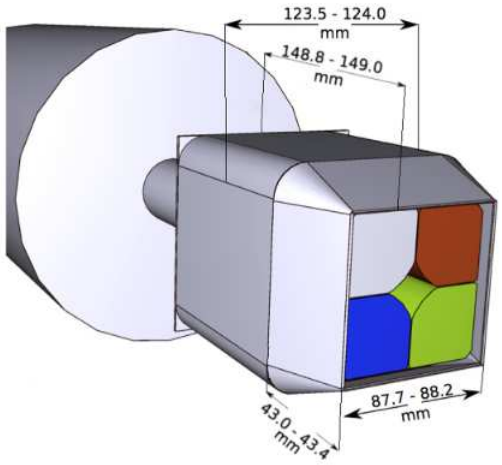

Figure 4.3: *Four Germanium clovers (having different colors) in GRIFFIN. [Rizwan et al., 2016].*

4.1.3 Additional Detectors in GRIFFIN

In the GRIFFIN rhombicuboctahedral setup, there are eight triangular faces alongside the 18 square faces containing HPGe detectors, beamline equipment, and tape systems. These triangular faces provide space for various additional detectors, including cerium-doped lanthanum bromide ($LaBr_3(Ce)$), shown in Fig. 4.4 detectors with approximately 5% Cerium concentration. The HPGe detectors offer excellent energy resolution but lack the fast nanosecond timing resolution required for precise fast-timing analyses of excited states. In contrast, the $LaBr_3(Ce)$ detectors have demonstrated the capability to determine lifetimes with a precision of approximately 10 ps. However, it is important to note that the absolute efficiency of the eight $LaBr_3(Ce)$ detectors in GRIFFIN at 1 MeV is relatively low, measuring only 1.8(1)%. [Garnsworthy et al., 2019]

Alongside GRIFFIN include the SCEPTAR, in Fig. 4.5, divided into two hemispheres, each containing 10 thin (1.6 mm) plastic scintillators. These scintillators are arranged into pentagonal rings and are primarily used for detecting β particles. SCEPTAR exhibits an efficiency of approximately 80%, making it highly effective for tagging β particles and improving the spectrum's cleanliness by rejecting room background signals. This setup enhances the ability to detect peaks that might otherwise be obscured by room background events, especially in $\beta-\gamma-\gamma$ coincidence events [Ball et al., 2005].

The DESCANT, in Fig. 4.6, is an array of detectors, consisting of 70 closely packed detectors filled with deuterated Benzene. DESCANT is primarily employed to study beta-delayed neutron emitters. It is positioned approximately 50 cm from the point where the beam is implanted, replacing the lampshade of GRIFFIN in the outgoing beam line direction. Additionally, DESCANT can be used in conjunction with the TIGRESS array for enhanced experimental capabilities [Garrett, 2014, Hackman and Svensson, 2014]. Other detectors are discussed by [Garnsworthy et al., 2019].

Figure 4.4: *$LaBr_3$ detector [Garnsworthy et al., 2019].*

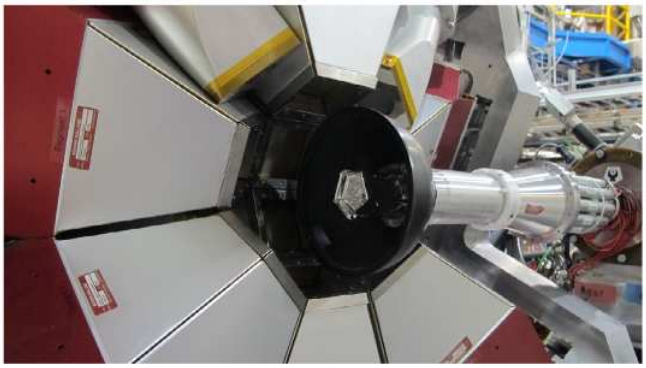

Figure 4.5: *SCEPTAR and BGO (red and sliver) around the HPGe [Garnsworthy et al., 2019].*

Figure 4.6: *DESCANT [Garnsworthy et al., 2019].*

4.2 S1723 experiment

The S1723 experiment, conducted at the TRIUMF facility in Canada, focuses on investigating the evolution of deformation in neutron-rich isotopes below ^{68}Ni. It utilizes clean Manganese (Mn) beams generated at ISAC-I and takes advantage of the GRIFFIN array's efficiency and the versatility of its ancillary detectors. The primary focus is on exploring the N = 40 Island of Inversion, with a specific emphasis on Fe, Co, and Ni isotopes. By conducting detailed spectroscopy of these nuclei, the research aims to rigorously test theoretical models describing not only the Island of Inversion but also the broader region, including phenomena like collectivity, deformation, and shape co-existence. The beam of ^{62,64,66}Mn is used to investigate the structural properties of potential isotopes within the Island of Inversion, namely,^{62,64,66}Fe. This thesis discussion exclusively focuses on the isotope ^{62}Fe. The analysis of the rest of the decay chain or other masses, is left for future work.

For this experiment, 5 out of the 16 GRIFFIN clovers were utilized, with the clover at position 13 removed to accommodate the PACES Dewar. SCEPTAR serves as a highly efficient detector for beta particles, with efficiency of approximately 80%, emitted during radioactive decays. The Germanium detectors are enclosed by BGOs, which function as a Compton suppression, see Fig. 4.5. $LaBr_3$ were also used during the experiment however, $LaBr_3$ and PACES have no part in the presented analysis.

At the ISAC facility, RIBs are generated using the ISOL technique at TRIUMF. The ISOL setup comprises a beam, target, mass separator, and beam transportation system. Initially, a proton beam, of 500 MeV with a 20 µA current [Svensson and Garnsworthy, 2014], from TRIUMF's cyclotron is used to create a wide range of isotopes through various nuclear reactions like spallation, fragmentation, and fission in suitable target materials. It is important to mention that in this experiment, the primary focus is on ^{62}Mn, which is generated through the process of fission. To select a specific isotope species from this mix, RILIS is employed. RILIS is a type of narrow-band laser. It typically uses a highly tunable and narrow-band laser to selectively excite and ionize specific atomic or isotopic species. The laser wavelength is precisely tuned to match the energy levels of the target species, allowing for highly selective ionization. This narrow-band laser approach is essential in RILIS to ensure that only the desired species are ionized while minimizing interference from other elements or isotopes in the sample. The potential difference accelerates the ionized isotopic species with energies between 20 keV and 40 keV [Garnsworthy et al., 2019]. Subsequently, all these isotopes are directed to the ISOL mass separator, where magnets apply Lorentz forces to separate and isolate the specific isotope of interest, which in this experiment is ^{62}Mn [Kunz et al., 2023, Baartman, 2014, Raeder et al., 2013].

The ^{62}Mn beam initially has very high intensity, but it needs to be significantly attenuated, by a factor of 100, to avoid overloading the DAQ. In the experiment, the GRIFFIN system begins by measuring the background radiation for 1 second. Afterward, there is a sequence involving a 15-second beam on, followed by a 2.5-second beam off, and a 1.5-second tape movement. This entire cycle is repeated periodically and the approximate total time for data collection during the experiment is 1 hour.

During the experiment, the GRIFFIN system first measures background radiation for 1 second. Subsequently, 15s beam on, 2.5s beam off, and the 1.5s tape movement. This tape cycle is periodically repeated

Chapter 5
Analysis and Results

5.1 Previous Experiments on ^{62}Fe

The ^{62}Fe nucleus was first sudied in Ref. [Runte et al., 1983], and was re-investigated by [Hoteling et al., 2010]. The study in [Hoteling et al., 2010], investigated the level structures in ^{60}Fe and ^{62}Fe isotopes. The experiment utilized Gammasphere and involved bombarding a ^{238}U target with a ^{64}Ni beam at an energy of 430 MeV [Lee, 1990]. High-spin level schemes were deduced through prompt coincidence events that were both singly- and doubly-gated. Additionally, levels resulting from the β decay of ^{60}Mn and ^{62}Mn isomers were examined using delayed coincidences, both singly- and doubly-gated [Hoteling et al., 2010].

The data analysis involved sorting the data based on the timing in relation to a beam burst. This sorting allowed for the construction of three-dimensional coincidence histograms (cubes), specifically the prompt (PPP) and delayed (DDD) coincidence cubes. Events in the PPP cube included γ-rays detected within a 40-ns window centered around the beam pulse. In contrast, the DDD cube included γ-rays originating from the radioactive or isomeric decay of nuclei resulting from nuclear reactions that occurred within 40 ns of each other, but outside the 40-ns window for prompt events [Hoteling et al., 2010]. The level scheme from the delayed and prompt are shown in Fig. 5.1 and Fig. 5.2 respectively.

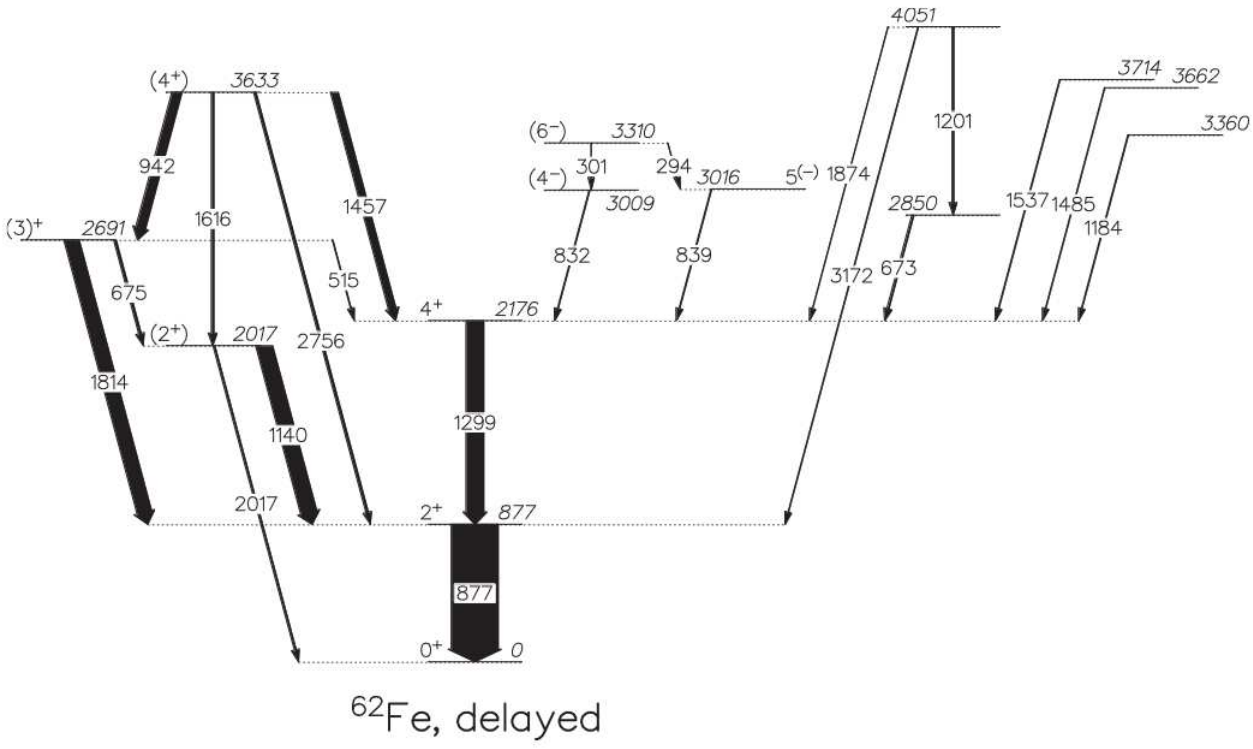

Figure 5.1: *The level scheme of ^{62}Fe from the delayed data. [Hoteling et al., 2010].*

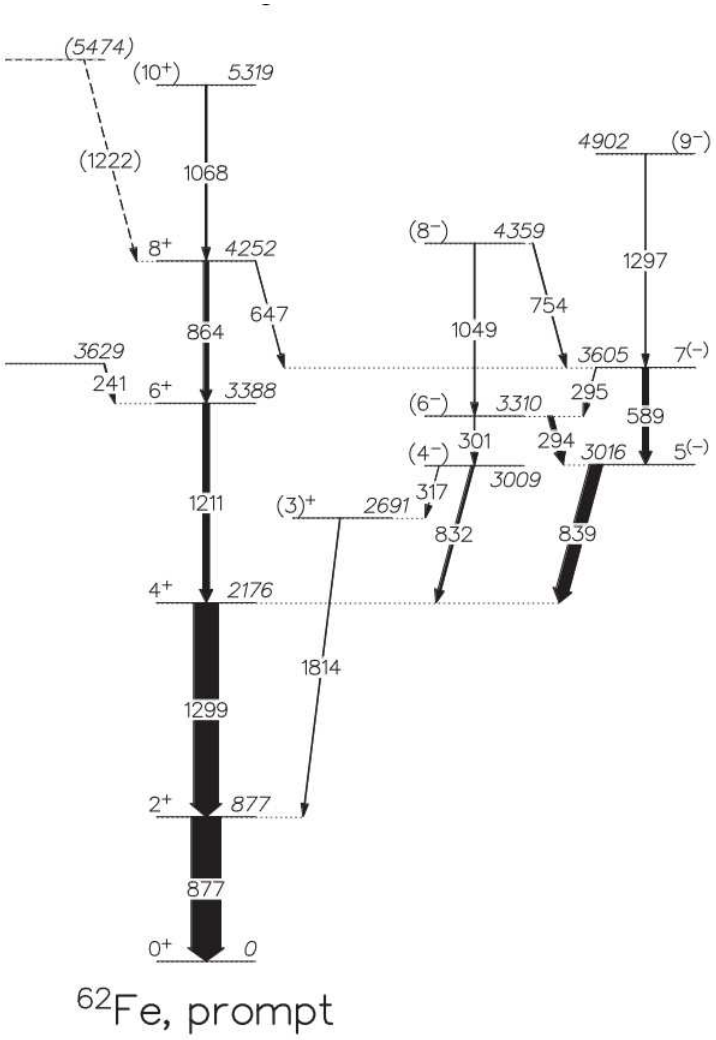

Figure 5.2: *The level scheme of ^{62}Fe from the prompt data. [Hoteling et al., 2010].*

5.2 Analysis of S1723 Experiment

In this section, the primary objective is to expand the ^{62}Fe level scheme using the data obtained, with a specific focus on identifying and documenting newly discovered gamma rays and energy levels. The data from the experiment is then unpacked and sorted using GRSISort [grs,], an analysis framework developed within the ROOT environment, Ref. [Brun and Rademakers, 1997] provides the details about ROOT. This sorted data is structured into fragment (singles) and analysis (coincidences) trees, which can be easily converted into histograms for further detailed analysis.

It is important to notice that ^{62}Mn has two β-decaying isomers, with spin 1^+ and 4^+. The ^{62}Mn beam delivered by ISAC contained a mix of both isomeric states, with an unknown ratio between them. The 1^+ isomer decays via β-decay, populating only three different levels: a 1691.0 keV level with a spin-parity of 0^+, an 877.0 keV level with a spin-parity of 2^+, and the ground level with a spin-parity of 0^+ of ^{62}Fe as shown in Fig. 7.1. On the other hand, the 4^+ isomer can populate a number of nuclear levels in ^{62}Fe as shown in Fig. 7.2. However, both states 1^+ and 4^+ decay independently of each other because they are two different states of two different nuclei. The newly established level scheme resulting from the analysis extensively discusses the decay of the two isomers to ^{62}Fe through the process of β-decay.

Before conducting the analysis, a careful check was performed to examine the energy spectrum of ^{62}Fe for potential contamination. Given the short lifetime of ^{62}Mn (of the order of ms for both isomers) as it implanted on the tape in GRIFFIN, it was crucial to confirm that it completely decays into ^{62}Fe,

the decay chain of ^{62}Mn can be seen in Fig. 5.3. This was crucial to ensure that the data exclusively represented the energy spectrum of ^{62}Fe. Given the longer lifetime of ^{62}Fe (68 seconds), there may be a possibility that some of it decays into other isotopes like ^{62}Co or ^{62}Ni. To confirm the purity of the energy spectrum, a thorough comparison was made between the energy spectrum of ^{62}Fe and the level schemes of ^{62}Co and ^{62}Ni, as well as the previously established ^{62}Fe level scheme. Even with a very short tap cycle of 15 s beam on and 2.5 s beam off, could not suppress the decay products of ^{62}Mn.

Figure 5.3: *The decay chain of the ^{62}Mn. This figure is taken from the NNDC.*

5.2.1 Efficiency

The analysis incorporates three distinct calibration sources: ^{152}Eu, ^{133}Ba, and ^{60}Co. To ensure accurate calibration, a dedicated script was employed to handle the calibration of these sources. This step was deemed crucial as it provided essential calibration information necessary for the subsequent data sorting process, ensuring the reliability of the analysis.

To cover the full range of (approximately 100 keV to 4000 keV) energies needed for the ^{62}Fe analysis, additional energy points; 833.5 keV, 1039.2 keV, 2189.6 keV, 2751.8 keV, and 4295.1 keV, from ^{66}Ga were included, in addition to those from ^{152}Eu and ^{133}Ba calibrations. In Figure 5.4, all energy points, including those of ^{152}Eu, ^{133}Ba, and ^{66}Ga, are combined and plotted against their corresponding efficiencies. In Figure 5.4, it is crucial to note that both energy and efficiency values are presented in a logarithmic (natural log) scale. The expression 5.1 provided in [Garnsworthy et al., 2019] is utilized for the calculation of efficiencies.

$$ln\varepsilon = \sum_{i=0}^{8} a_i \left[ln(E_\gamma)\right]^i \tag{5.1}$$

The efficiency fitting function illustrated in Fig. 5.4 functions effectively for the majority of energy values. However, it exhibits imperfections for energies below 121 keV, which implies that energy values below this threshold are not reliable. Nevertheless, it is noteworthy that in our analysis, we did not

encounter any energy values lower than 240 keV. This suggests that the selected fitting function, a polynomial of degree 8, is well-suited for the relevant energy range of the study, providing satisfactory results.

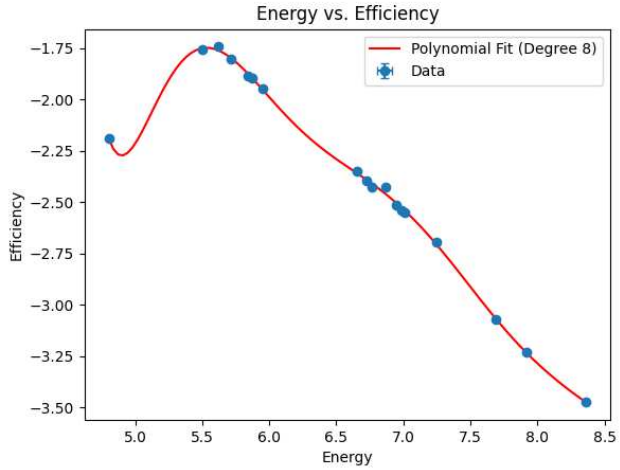

Figure 5.4: *Absolute Efficiency as a function of energy of* ^{152}Eu, ^{133}Ba, *and* ^{66}Ga *fitted to the polynomial of degree 8. Both energies and efficiencies are in natural log scale.*

5.2.2 Gamma-Ray Spectra

In the analysis, the energy spectrum of detected gamma rays from the HPGe detector is presented in three parts, as illustrated in Fig. 5.6, Fig. 5.7, and Fig. 5.8. These figures highlight the major peaks in the gamma spectra. Fig. 5.7 displays a peak at 1172 keV, corresponding to ^{62}Ni, indicating a decay product of ^{62}Mn, the decay chain of ^{62}Mn can be seen in Fig. 5.3. Furthermore, Fig. 5.9 represents the γ-γ matrix gated on the 814 keV gamma, resulting form the decay of the 1^{62} isomer, has a strong coincidence with the 877 keV gamma. Often in the gamma detection process, it is common that a gamma of specific energy to be detected in one detector, lose some of its energy due to Compton scattering, and then deposit the remaining energy in another detector. This results in the creation of a Compton diagonal in the energy spectra, as illustrated in Figure 5.5. Any two random points on a diagonal line add up to the energy of that specific gamma ray. These events are not real γ-γ coincidences but rather represent a Compton background. To address this, the analysis employs the TBGSubtraction class in GRSIsort, which subtracts this Compton background by setting gates, as shown in Fig. 5.10, on both the higher and lower parts of the Compton diagonal. The real γ-γ coincidences occur at the intersecting points where vertical lines (representing gammas of different specific energies detected in one detector) intersect horizontal lines (representing gammas of different specific energies) meets. The lines are actually the Compton background of those gammas. For instance, the coincidence of the 877 keV gamma with other energies like 1139 keV and 1298 keV is visually represented as vertical and horizontal lines. As mentioned these lines are actually the Compton background of these gammas. For instance, the intersection at 877 keV on both the x-axis and y-axis does not indicate gamma-gamma coincidence but rather gamma-Compton (or Compton-gamma) coincidence. This signifies the simultaneous detection of a full-energy 877 keV gamma and a Compton event depositing 877 keV but originating from a gamma of higher energy (e.g., 1139 keV or gamma from another energy level), as illustrated in Fig. 5.5. However, it is worth noting that sometimes the Compton background is not completely subtracted, and a very small portion of it may remain, manifesting as a negative peak in the spectrum (below 0 on the y-axis), as observed in Fig. 5.8.

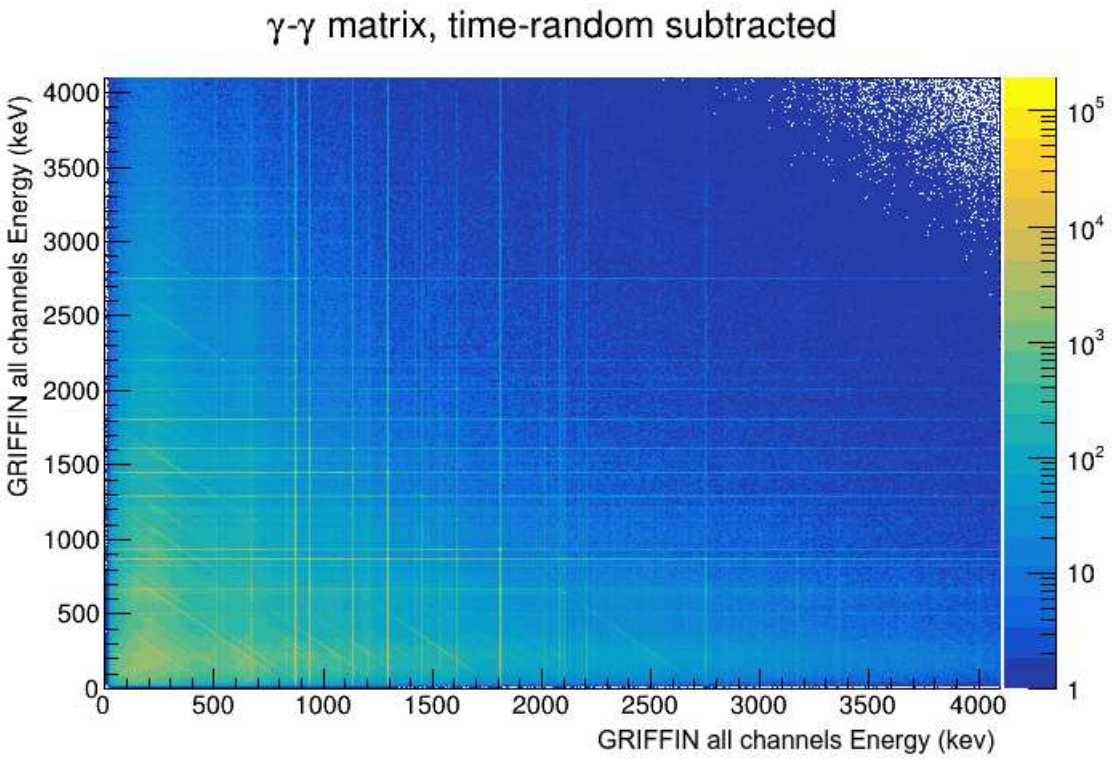

Figure 5.5: *The diagonal lines in the figure represent Compton diagonals. Additionally, the figure illustrates the coincidence of a single gamma ray with several other gamma rays.*

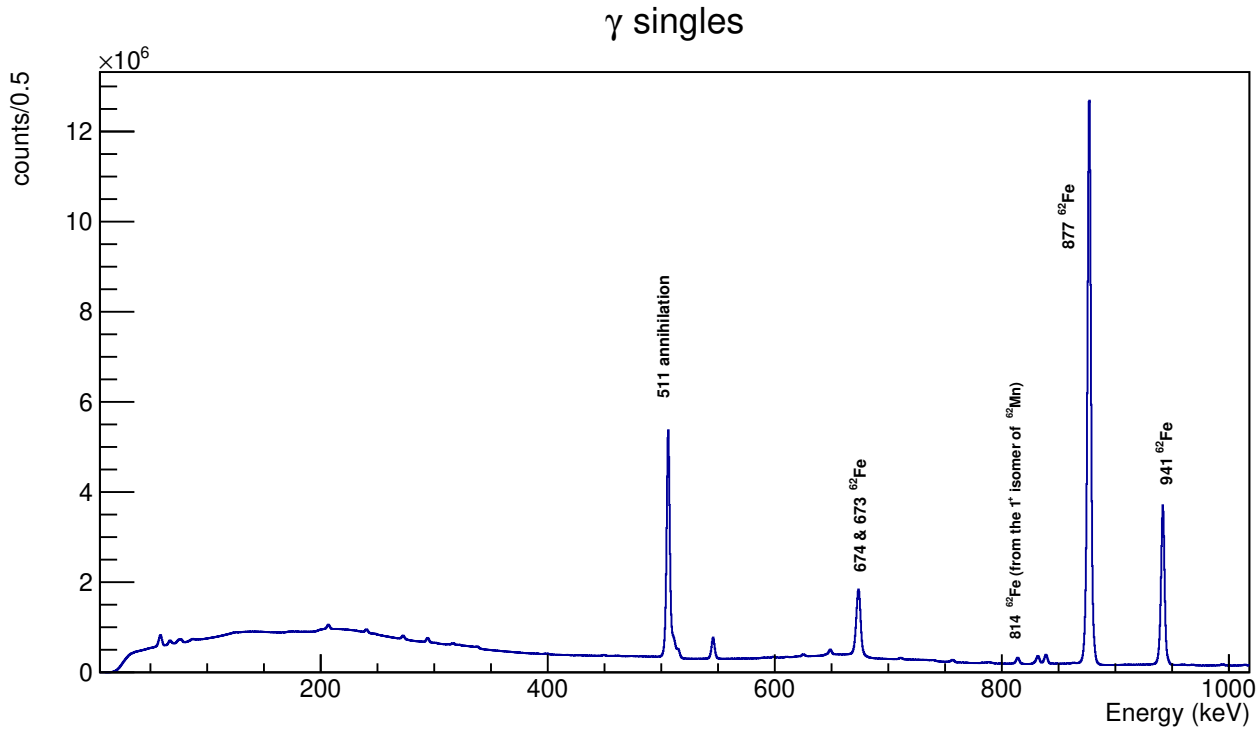

Figure 5.6: *γ-ray spectra between 0 and 1000 keV seen by the GRIFFIN HPGe clover detectors. This figure represents the singles γ-ray spectrum. The 814 keV gamma is important as it is from the level scheme obtained from the decay of 1^+ ^{62}Mn isomer.*

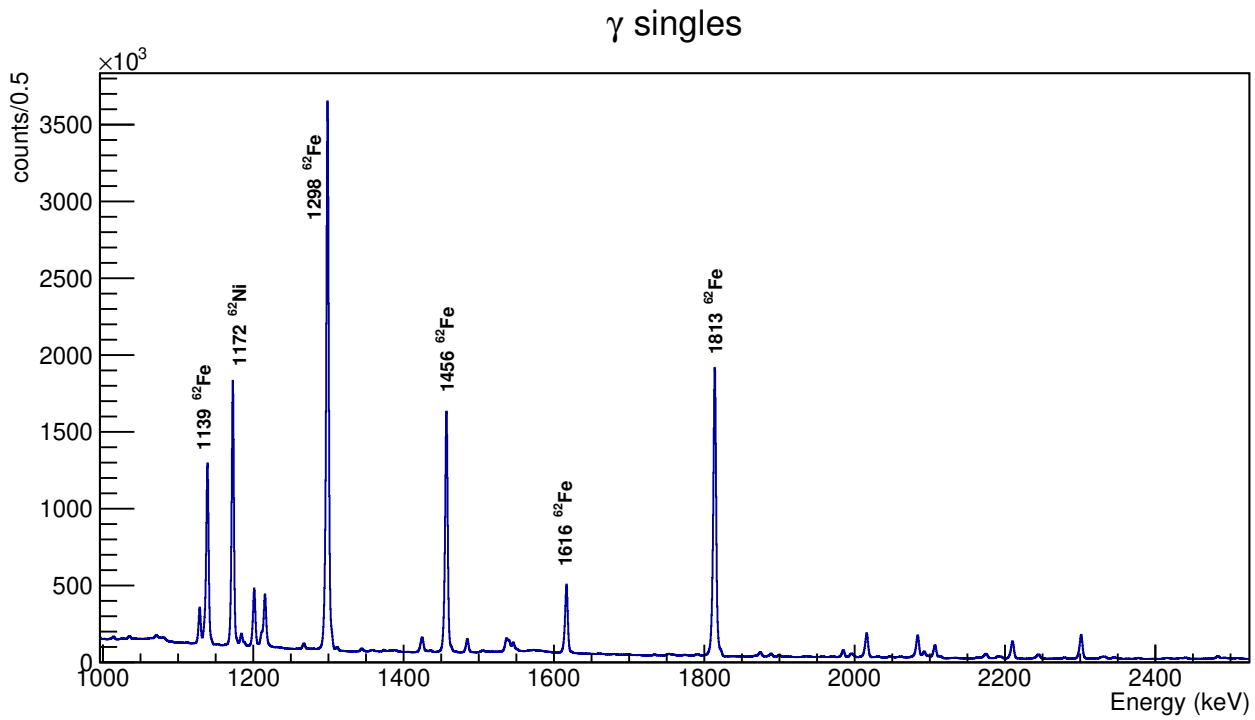

Figure 5.7: *γ-ray spectra between 1000 and 2500 keV seen by the GRIFFIN HPGe clover detectors. This figure represents the singles γ-ray spectrum. The presence of decay product of* ^{62} *can also be seen in this figure, the 1172 keV peak corresponding to* ^{62}*Ni.*

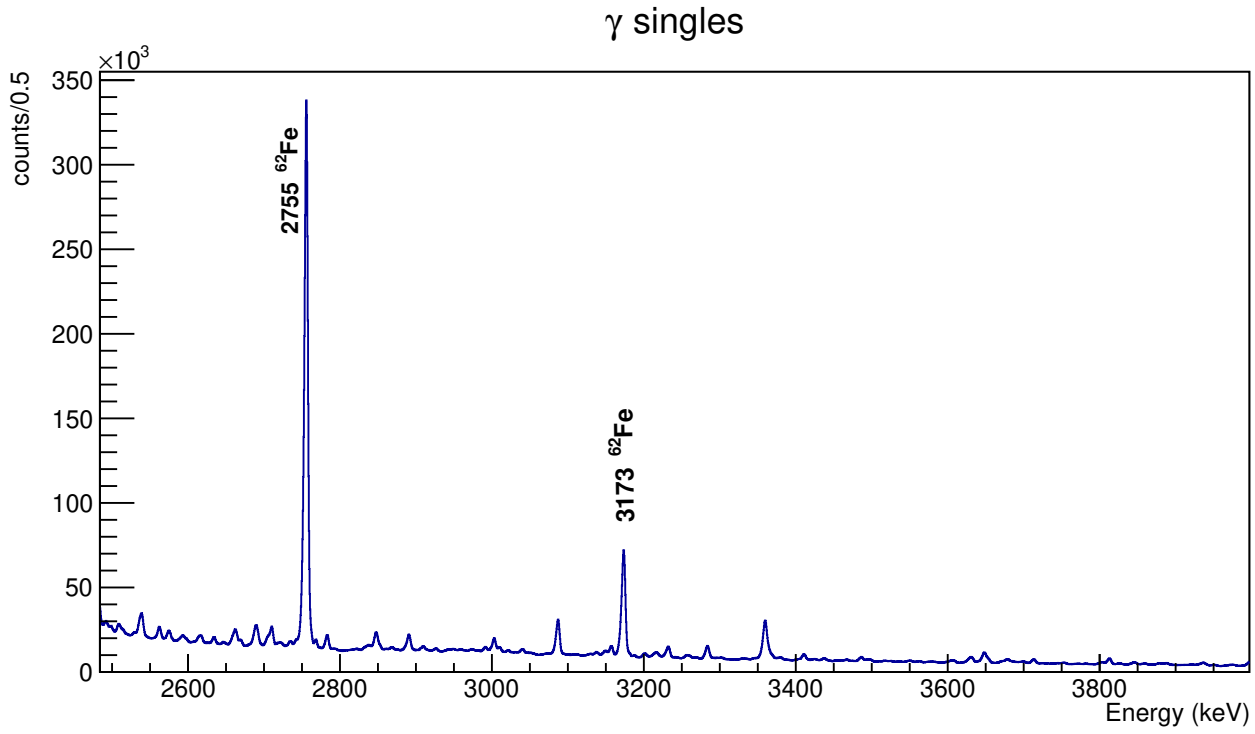

Figure 5.8: *γ-ray spectra between 2500 and 4000 keV seen by the GRIFFIN HPGe clover detectors. This figure represents the singles γ-ray spectrum.*

5.2.3 Results

The ISAC beam used in the experiment consists of a mixture of the 1^+ and 4^+ isomers of ^{62}Mn. As a result, when these isomers decay into ^{62}Fe, two distinct level schemes are formed. While it

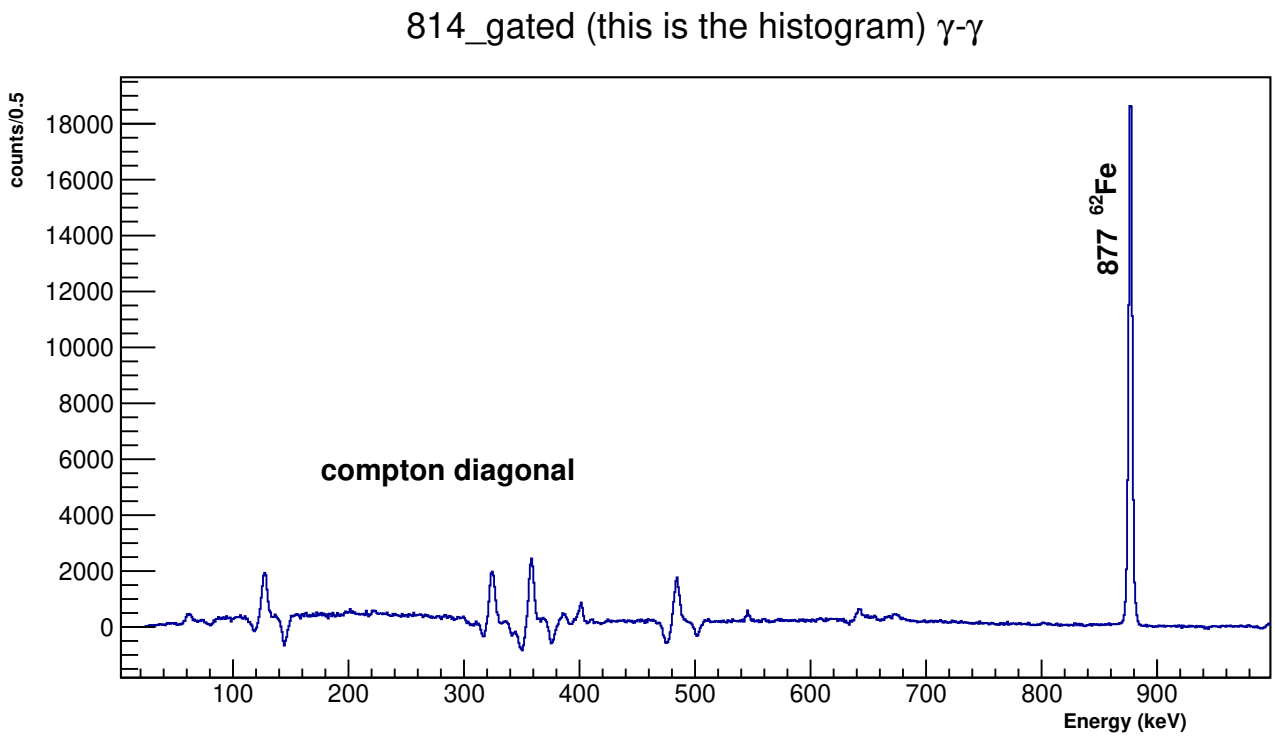

Figure 5.9: *When gated on the 814 keV, it is in with the coincidence with the 877 keV which can be seen in this figure obtained from the γ-γ matrix. The Compton diagonal can also be seen in this figure.*

is challenging to provide precise proportions of the two isomers in the beam, existing knowledge from a prior study by [Hoteling et al., 2010] and the newly established level scheme from the S1723 experiment, a rough estimation can be made that over 90% of the decays are associated with the 4^+ isomer, while less than 10% involve the 1^+ isomer. This estimation is based on the intensity which is future explained at the end of 5.2.4

The Decay of 4^+ Isomer of ^{62}Mn to ^{62}Fe

In the data analysis, the TBGSubtraction class was utilized, taking the AddBack factor into account. Add Back, in gamma-ray spectroscopy, refers to the process of combining the energy deposits from a single gamma-ray event that is detected in multiple crystals in a single clover. This technique involves summing the energy recorded in each crystal to reconstruct the full energy of the γ-ray, which may be partially absorbed in one crystal and detected in another. The add-back process helps improve the accuracy and completeness of gamma-ray energy measurements in multi-crystal detector systems. When dealing with peak fitting in GRSIsort, the Gaussian function is no longer suitable, and instead, the option of TABPeak (a specialized function designed for fitting add-back peaks) should be selected within the TBGSubtraction, see Fig. 5.10. Gating on a specific energy peak and the corresponding coincidences are observed in the right window. This information is then saved as a histogram for subsequent analysis.

During the analysis, a number of new energy levels and γ-ray transitions were discovered. These findings have expanded upon the previously known level scheme, as shown in the Appendix Fig. 7.2. Particular attention was given to the intense gamma transitions with energies of 877.3 keV, which exhibited the highest intensity of 98%, along with gammas at 1139.8 keV, 1299.2 keV, 1814.0 keV, 941.8 keV, and 1457.1 keV, in Fig. 7.2. The analysis involved gating on the mentioned energies and searching for additional gammas in the data. The new level scheme for ^{62}Fe, particularly of the 4^+ isomer, has been divided into three parts for better clarity. The first part of the level scheme is presented in Fig. 5.12, the second part in Fig. 5.13, and the third part in Fig. 5.14. The transitions among different levels are presented in Table 5.1 and 5.2 (the table was too long and was therefore

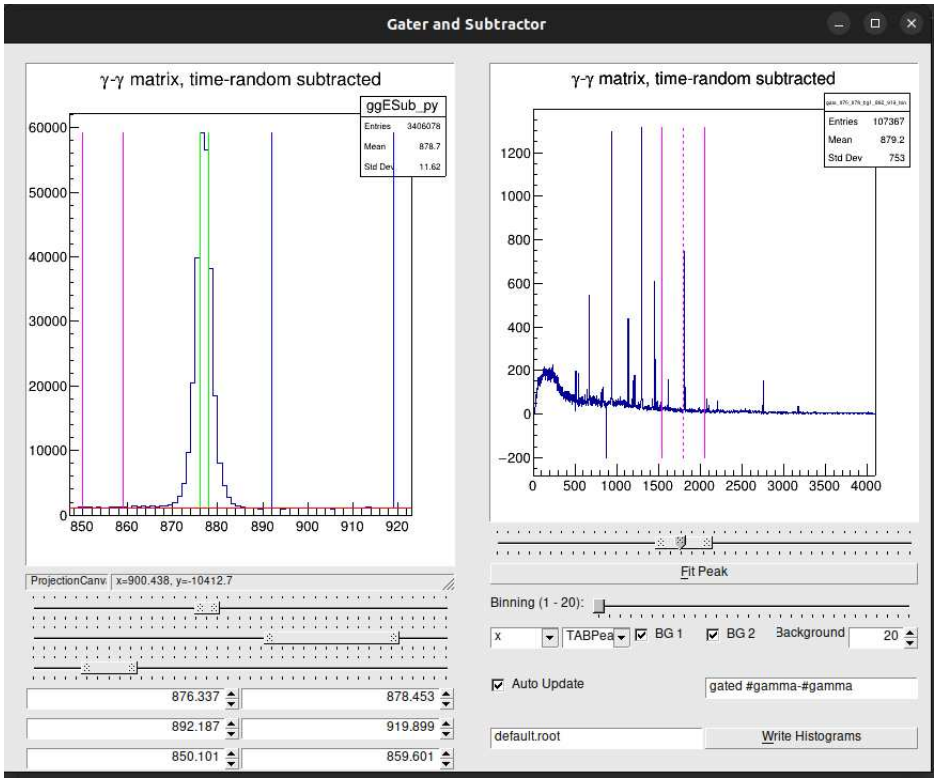

Figure 5.10: *The program output displays a γ-γ matrix seen by the GRIFFIN HPGe clover detectors on the left side of the window. The right window demonstrates the result of gating on a particular (here it is gated on the 877 keV peak) energy peak in the left window, providing the corresponding γ-γ coincidence events for that specific energy peak. The analysis utilized the TABPeak option, with BG1 and BG2 backgrounds selected. The gate on the peak is in green, while BG1 and BG2 are indicated in blue and purple, respectively in the left window. In the right window there is also a gate with a dotted line at the center which is used to get the area and the centroid of a peak in the right window.*

divided into two sections). In both tables, the newly discovered gamma transitions and the energy levels are highlighted in orange, while gamma transitions and energy levels from the previous level scheme, for the 4^+ isomer are shown in black. Additionally, a specific value in Table 5.2 is highlighted in dark green, indicating uncertainty regarding its position as it appeared in different levels.

The Decay of 1^+ isomer of ^{62}Mn to ^{62}Fe

The level scheme resulting from the decay of the 1^+ isomer of ^{62}Mn to ^{62}Fe is presented in Fig. 5.11. When analyzing the gamma transitions, it was observed that when the analysis was focused on the 877.0 keV gamma, a corresponding gamma transition at 814.0 keV was observed in coincidence. Conversely, when gated on the 814.0 keV gamma transition, it also exhibited a strong coincidence with the 877.0 keV gamma transition. This consistency aligns with the previously established level scheme from the decay of the 1^+ isomer of ^{62}Mn to ^{62}Fe.

It is noteworthy that the previously reported gamma transitions and energy levels, from the decay of the 1^+ and 4^+ isomers of ^{62}Mn to ^{62}Fe are consistent with the results of this analysis, see Table 5.1 and 5.2. In the analysis, absolute intensities and their associated uncertainties were calculated. By inputting detailed information about both the parent nucleus (^{62}Mn) and the daughter nucleus (^{62}Fe) into the NNDC [log,], lead to the determination of Log(ft) values associated with each energy level in ^{62}Fe. Table 5.3 presents a summary of the potential spin-parity assignments for the newly identified energy levels. The determination of whether a beta decay is allowed or forbidden, and determining the specific type of forbidden decay, for the newly discovered energy levels is inconclusive based on their Log(ft) values. This uncertainty arises because the Log(ft) values for these levels fall within the

overlapping range of both allowed and forbidden transitions, as seen in the comparison with Fig. 3.4 and Fig. 3.5.

Table 5.1: *Section I: Newly discovered gamma transitions and energy levels are marked in orange, while gamma transitions and energy levels from the previous level scheme are indicated in black. An uncertain gamma transition is highlighted in dark green.*

Energy	**Initial State**	**Final State**	**Intensity**
876.9	877.0	0.0	92 (6)
1139.03	2016.2	877.0	11 (3)
2015.89	2016	0.0	3 (1)
1215.47	2092.6	877.0	3 (1)
2092.31	2092.6	0.0	0.9(4)
1298.74	2175.8	877.0	36 (11)
240.4	2415.8	2175.8	0.20 (1)
515.09	2690.8	2175.8	0.8 (1)
674.75	2690.8	2016.2	4 (1)
1813.7	2690.8	877.0	29 (13)
673.3	2849.2	2175.8	5.0 (8)
959.6	2975.8	2016.2	0.10 (2)
967.7	2983.9	2016.2	0.10 (2)
831.7	3007.5	2175.8	1.2 (2)
838.9	3014.6	2175.8	1.3 (2)
994.4	3086.8	2092.6	1.4 (3)
1070.8	3086.8	2016.2	0.200 (3)
2209.8	3086.8	877.0	14 (1)
3086.67	3086.8	0.0	4 (2)
294.2	3308.8	3014.6	0.3 (2)
301.7	3308.8	3007.5	0.4 (4)
1184.16	3360.1	2175.8	0.7 (1)
1343.9	3360.1	2016.2	0.20 (5)
1210.8	3386.6	2175.8	0.6 (1)
1423.3	3439.1	2016.2	0.4 (1)
1266.1	3442.1	2175.8	0.5 (1)

Table 5.2: *Section II: Newly discovered gamma transitions and energy levels are marked in orange, while gamma transitions and energy levels from the previous level scheme of ^{62}Fe are indicated in black. An uncertain gamma transition is highlighted in dark green.*

Energy	Initial State	Final State	Intensity
610.6	3459.3	2849.2	0.9 (9)
1425.1	3600.8	2175.8	0.8 (3)
625.1	3632.4	3007.5	0.3 (2)
545.6	3632.4	3086.8	1.2 (2)
941.8	3632.4	2690.8	26.9 (7)
1456.9	3632.4	2175.8	18 (6)
1616.5	3632.4	2016.2	6 (2)
2755.4	3632.4	877.0	9 (5)
1484.6	3660.4	2175.8	0.9 (3)
1266.1	3682.1	2415.8	0.5 (1)
1867.8	4043.6	2175.8	0.10 (5)
449.5	4050.5	3600.8	0.10 (9)
1201	4050.5	2849.2	3.1 (8)
1874.6	4050.5	2175.8	0.5 (2)
3173.5	4050.5	877.0	2 (1)
1936.9	4112.6	2175.8	0.20 (6)
1984.9	4160.7	2175.8	0.5 (2)
1545.6	4236.4	2690.8	0.6 (2)
1899.5	4590.3	2690.8	0.3 (1)
1014.4	4674.8	3660.4	0.1 (1)
2047.3	4738.1	2690.8	0.20 (9)
2351.5	4767.1	2415.8	0.1 (1)
1888.9	5348.2	3459.3	0.4 (1)
1998.4	5348.2	3386.6	0.4 (1)
2377.7	5978.5	3600.8	0.1 (1)
2689.0	6321.0	3632.4	0.10 (6)

5.2.4 Assigning Spin-Parity

The comprehensive selection rules are outlined in Table 3.1, Table 3.4, and Equation 3.64 from Chapter 3. These rules provide invaluable guidance for our spin-parity assignments.

In the case of the 4^+ isomer of ^{62}Mn decaying and populating various levels in ^{62}Fe, the assignment of spin-parity for different levels is discussed below.

- The ground state of ^{62}Mn, with a spin-parity of 4^+, can populate the 2092.6 keV excited state in ^{62}Fe. From Fig. 5.12 it can be observed that the 2092.6 keV level transitions: one to the 877.0 keV excited state with a spin-parity of 2^+ and another to the ground state with a spin-parity of 0^+. No transitions were observed to 4^+ states. From this information and using the selection rule for gamma transitions (Equation 3.64), it is estimated that the possible spin-parity of the 2092.6 keV level is either 1^+ or 2^+. All similar energy levels in the newly established levels scheme that only have a transition to both 2^+ and 0^+ will have the spin-parity of either 1^+ or 2^+.

- The 2415.8 keV excited level in ^{62}Fe, has only one transition to the 4^+ level, at 2175.8 keV in ^{62}Fe as shown in Fig. 5.12. From the possible values we get from the selection rules for the gamma transition, we do not see that the 2415.8 keV is populating any of the lower-lying 2^+ states. As a result, the possible spin-parity for this level is narrowed down to either 5^+ or 6^+. The energy levels that exhibit a transition to only 4^+ state in ^{62}Fe will have a potential spin-parity of either 5^+ or 6^+.

- The 2975.8 keV undergoes gamma transition decays to only 2016.2 keV excited level, which has a spin-parity of 2^+. The possible spin-parity for the 2975.8 keV level can be either 3^+ or 4^+. Since no transition is observed to the 0+ state (ground state), helps us to eliminate the possibility of angular momentum of 2^+ or lower. All levels that have a transition exclusively to the 2^+ state in the ^{62}Fe nucleus can have a possible spin-parity of 3^+ or 4^+.

- For the 3459.3 keV excited level in ^{62}Fe, the possible spin-parity for this excited level can only be 7^+. It only presents one transition to the 2849.2 keV level, which has two possible spin-parities of 5^+ and 6^+ and its transition to the other levels (lower than 4) are highly unlikely. Consequently, levels that have a transition only to 5^+ or 6^+ will have a possible spin-parity of 7^+ in the ^{62}Fe nucleus.

Additional analysis is needed to precisely determine the spin-parity values associated with each level in ^{62}Fe.

In the analysis, an unusual behavior was noticed among certain energy levels. The 3360.1 keV level can have either a 3^+ or 4^+ spin-parity configuration. A gamma transition with an energy of 1343.9 keV, exhibiting a mixed multipolarity of M1+E2, can populate the 2016.2 keV level, which has a 2^+ spin-parity configuration. Below this level, there is an 887.0 keV level with a 2^+ spin-parity configuration. From the level scheme in Fig. 5.12, the 3360.1 keV level is not populating the 887.0 keV, a 2^+ level. Further analysis would be needed to fully understand the specific reasons for this behavior. A similar pattern is observed for the transition between the levels 3439.1 keV and 2016.2 keV, and for the transition between the levels 3632.4 keV to 2016.2 keV.

Table 5.3: *The Energy levels, with new levels marked in orange and previous ones in black. It also includes information about their associated beta values, Log(ft) values, angular momentum, and parity.*

Energy Level	**Beta Value**	**Log*(ft)***	**L^{π}**
877.0	<14	>6.01 (6)	2^+
2016.2	3 (4)	6.3 (6)	(2^+)
2092.6	3 (1)	6.4 (16)	$(1^+,2^+)$
2175.8	<19	6.1 (10)	(4^+)
2415.8	<1.2 (0.18)	>7.8 (4)	$(5^+,6^+)$
2690.8	<19	5.9 (10)	(3^+)
2849.2	1 (2)	6.7 (5)	$(5^+,6^+)$
2975.8	0.10 (2)	7.7 (4)	$(3^+,4^+)$
2983.9	0.10 (2)	7.7 (4)	$(3^+,4^+)$
3007.5	0.6 (6)	6.8 (4)	(4^-)
3014.6	1.0 (4)	6.6 (4)	(5^-)
3086.8	<6.5	6.1 (5)	$(1^+,2^+)$
3308.8	0.6 (5)	6.8 (4)	(6^-)
3360.1	0.2 (1)	7.2 (4)	$(3^+,4^+)$
3386.6	0.2 (3)	7.2 (4)	$(5^+,6^+)$
3439.1	<1.4	6.9 (11)	$(3^+,4^+)$
3442.1	0.5 (1)	6.8 (4)	$(5^+,6^+)$
3459.3	<1.6	6.7 (4)	(7^+)
3600.8	0.6 (4)	6.7 (4)	$(5^+,6^+)$
3632.4	61 (8)	4.7 (7)	(4^+)
3660.4	0.8 (4)	6.5 (4)	$(5^+,6^+)$
3682.1	0.5 (1)	6.7 (4)	(7^+)
4043.6	0.1 (1)	7.4 (4)	$(5^+,6^+)$
4050.5	6 (1)	5.5 (9)	$(3,4^+)$
4112.6	0.2 (1)	7.0 (4)	$(5^+,6^+)$
4160.7	0.5 (2)	6.6 (4)	$(5^+,6^+)$
4236.4	0.6 (3)	6.5 (4)	$(4^+,5^+)$
4590.3	0.3 (1)	6.71 (4)	$(4^+,5^+)$
4674.8	0.1 (1)	7.2 (4)	(7^+)
4738.1	0.2 (1)	6.8 (4)	$(4^+,5^+)$
4767.1	0.1 (1)	7.1 (4)	(7^+)
5348.2	1 (1)	6.0 (7)	$(8^+,9^+)$
5978.5	0.1 (1)	6.7 (4)	(7^+)
6321.0	0.10 (5)	6.5 (4)	$(5^+,6^+)$

Table 5.4: *The Energy levels and the gamma transition from the decay of the y isomer of ^{62}Mn to ^{62}Fe It also includes information about their associated beta values, Log(ft) values, angular momentum, and parity.*

Energy Level	**Beta Value**	**Log(*ft*)**	**L^{π}**
877.0	-	-	2^+
814.0	0.6	-	(0^+)

As mentioned before, the experiment involved a beam composed of a mixture of the 4^+ and 1^+ isomers of ^{62}Mn, with no precise information on the proportion of each isomer in the beam, a rough estimate is that approximately 90% of the decay is attributed to the 4^+ isomer, while less than 10% involves the 1^+ isomer. The estimate that there are less than 10% of the 1^+ comes from the very small intensity of the 814 keV transition. The level scheme resulting from the decay of the 4^+ isomer of ^{62}Mn provides valuable information to understand the overall process. However, the information that can be extracted from the level scheme originating from the decay of the 1^+ isomer, Table 5.4 provides crucial information in the form of a beta value of 0.6. This indicates that the mixture containing both isomers, 0.6% of it can undergo β-decay, resulting in the population of the 0^+ 1691.0 keV level. The transition of this level to 877 keV is very small. The level schemes from the two different isomers of ^{62}Mn share the 877.0 keV level. However, due to a very small intensity of the 814 keV gamma populating the 877 keV, the 877 keV level is highly populated by the 4^+ and therefore we have no good information of how much of the 1^+ have populated the 877 keV level. The same argument holds for the ground state since the ground state is highly populated by the 4^+. In conclusion, the Log(ft) and beta values associated with the 877.0 keV level and the ground state in the decay of the 1^+ isomer has no significance due to their highly probable population by the 4^+ isomer, as indicated by the small intensity of the 814 keV gamma.

The isotope 62Fe does not fall within the Island of Inversion at N=40. 62Fe, with its 26 protons and 36 neutrons, does not exhibit the characteristic features of the Island of Inversion (N = 40) as shown in [Lenzi et al., 2010].

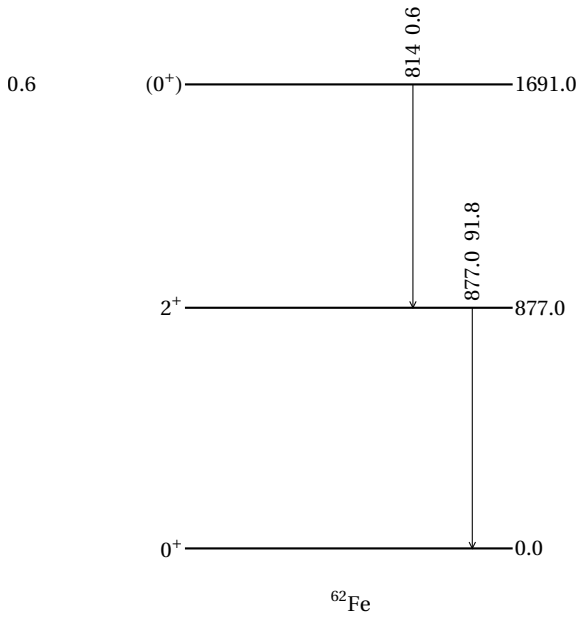

Figure 5.11: *The ^{62}Fe level scheme from the decay of 1^+ isomer of ^{62}Mn to ^{62}Fe, derived from the S1723 experiment. The only gamma 814 keV is in the strong coincidence with the 877.0 keV gamma. This level scheme is consistence with the previous level scheme.*

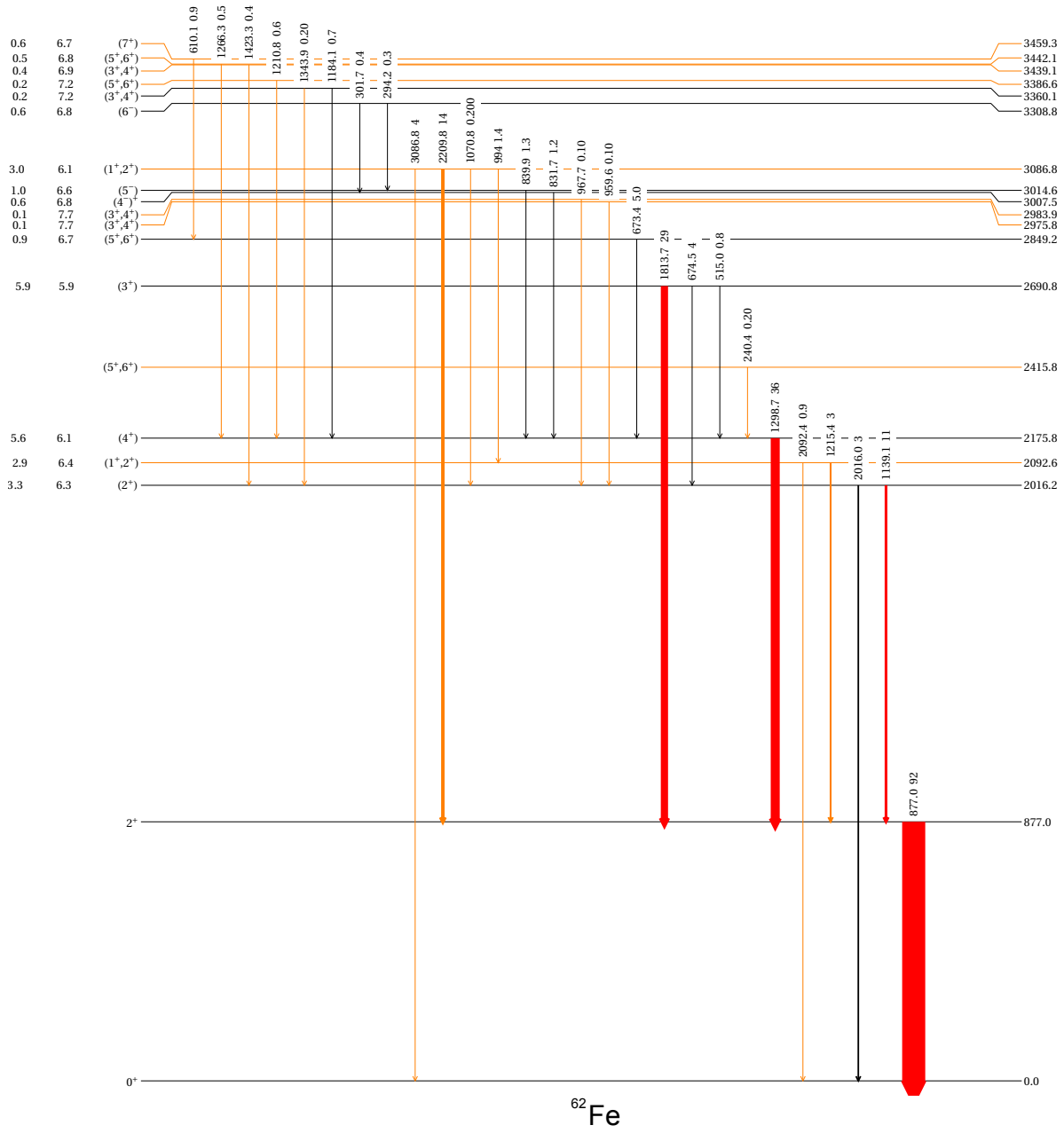

Figure 5.12: *The ^{62}Fe level scheme, derived from the S1723 experiment, displays newly discovered gamma rays in orange, while black indicates gammas from the previous level scheme. Red is used for the most intense gammas, and blue for the next most intense ones. Additionally, for the energy levels, new ones are in orange, and old ones are in black.*

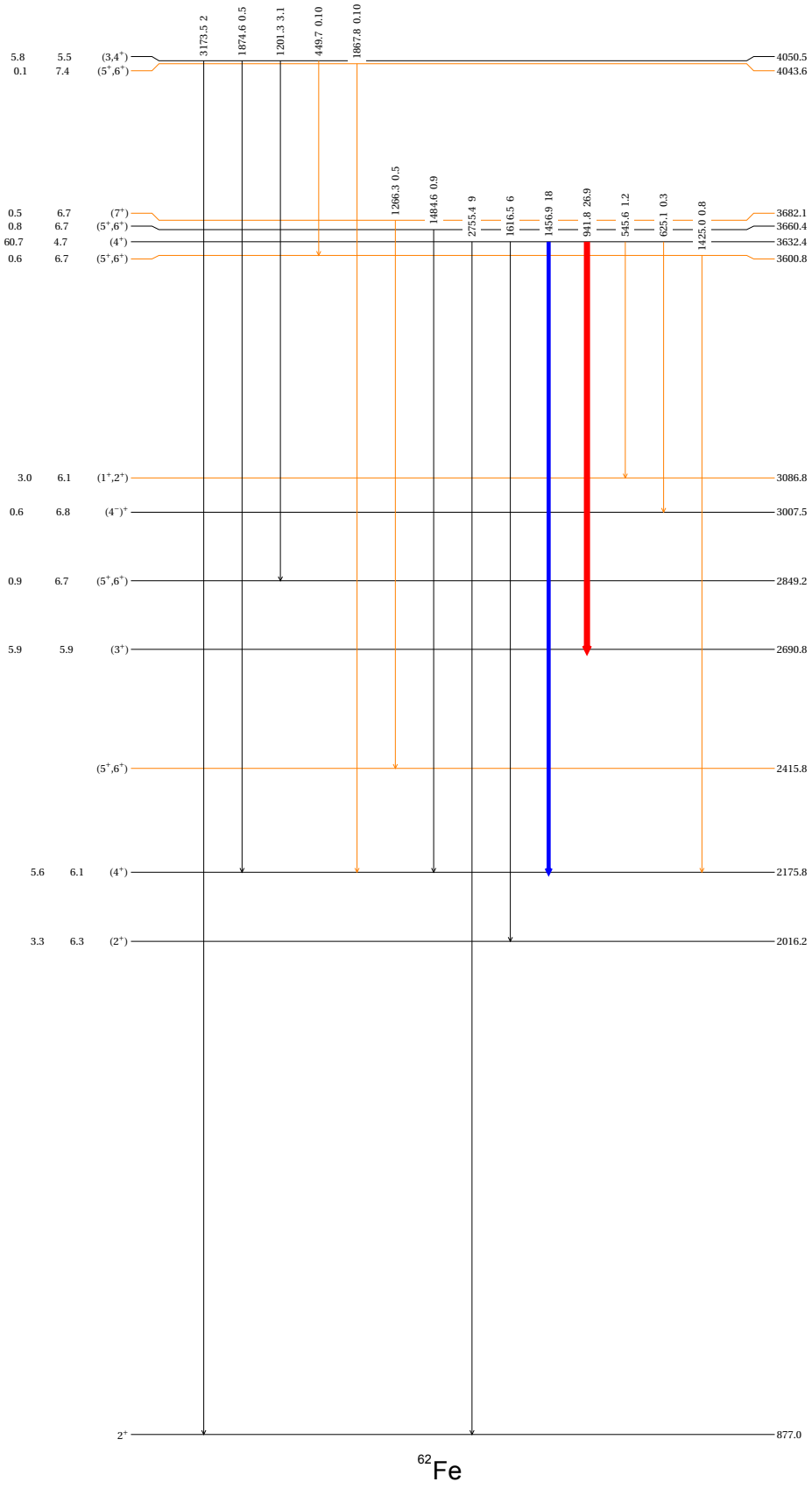

Figure 5.13: *The ^{62}Fe level scheme, derived from the S1723 experiment, displays newly discovered gamma rays in orange, while black indicates gammas from the previous level scheme. Red is used for the most intense gammas, and blue for the next most intense ones. Additionally, for the energy levels, new ones are in orange, and old ones are in black.*

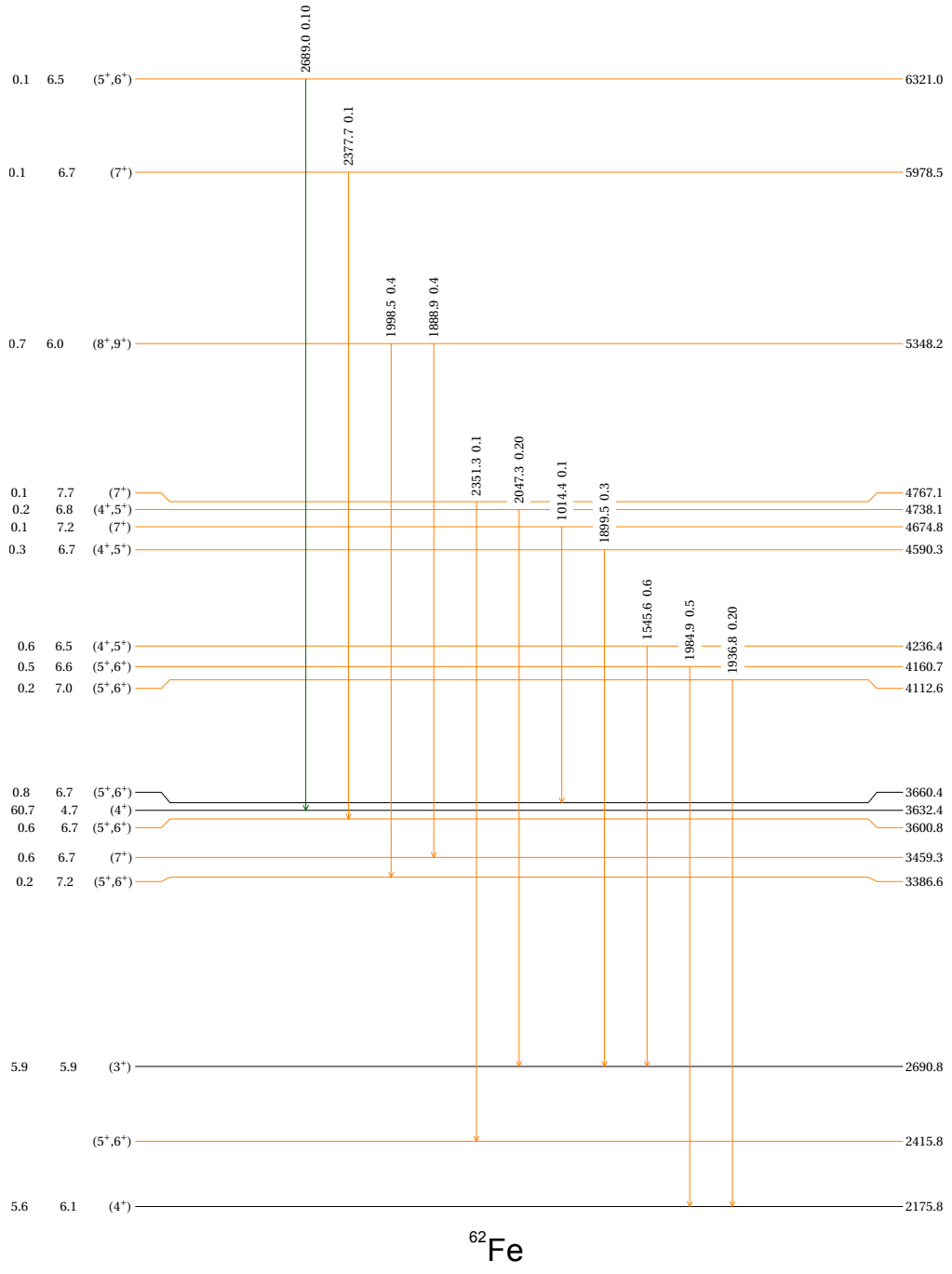

Figure 5.14: *The ^{62}Fe level scheme, derived from the S1723 experiment, displays newly discovered gamma rays in orange, while black indicates gammas from the previous level scheme. Red is used for the most intense gammas, and blue for the next most intense ones. Additionally, for the energy levels, new ones are in orange, and old ones are in black.*

Chapter 6
Conclusion & Future Work

The data from the S1723 experiment conducted at the TRIUMF facility in Canada provided high-quality data for the analysis of the ^{62}Fe nucleus. This analysis aimed to expand upon the existing level scheme of ^{62}Fe, which had been previously studied by [Hoteling et al., 2010]. Furthermore, the isotope 62Fe, with 26 protons and 36 neutrons, does not belong to the Island of Inversion at N = 40. Although 62Fe is on the border of this region, it provides valuable insights for understanding nuclear behavior in the vicinity of the Island of Inversion. During the analysis, 31 new gamma transitions and 22 new energy levels were successfully discovered in the ^{62}Fe nucleus, resulting from the decay of the 4^+ isomer of ^{62}Mn, shown in Fig. 5.12, Fig. 5.13, and Fig. 5.14. However, no new gamma transitions or energy levels were observed to be populated from the decay of the 1^+ isomer of ^{62}Mn to ^{62}Fe as shown in Fig. 5.11. This lack of new findings was consistent with the previously established level scheme from the prior study. Furthermore, the isotope ^{62}Fe, with 26 protons and 36 neutrons, does not belong to the Island of Inversion (N = 40), a region in the nuclear chart characterized by changing magic numbers for protons and neutrons. This means that ^{62}Fe's nuclear properties do not exhibit the unique behavior seen in isotopes within the Island of Inversion (N = 40). Although ^{62}Fe is on the border of this region, it provides valuable insights for understanding nuclear behavior in the vicinity of the Island of Inversion.

During the analysis, a significant focus was placed on the most intense gamma transitions from the previous level scheme, particularly the 877 keV, 1139 keV, 1299 keV, 1814 keV, 941 keV, and 1457 keV gammas. All the new gamma transitions and energy levels were obtained in coincidence with these key gamma transitions, helping to build an extended and more detailed level scheme for ^{62}Fe. A significant modification was made to the 1139 keV gamma transition. In the previous level scheme, shown in Fig. 7.2, this gamma had an absolute intensity of 34%, but it was adjusted to have an intensity of 11% in the new level scheme of ^{62}Fe. This change resulted in a considerable reduction in the intensity of the 1139 keV gamma transition in the new level scheme shown in Fig. 5.13. The gamma transitions and energy levels from the previous level scheme are consistent with those in the new level scheme. Additional investigation is required to gain a deeper understanding of the nuclear structure of ^{62}Fe. Some γ-rays from the analysis have not been definitively placed within the level scheme. A more comprehensive analysis, including an in-depth γ-γ coincidence study, is essential to fully understand the nuclear structure of this ^{62}Fe. Moreover, further analysis is required to determine the precise spin-parity and the type of beta decay for each energy level in the new level scheme. In future analyses, we can explore angular correlation studies to gain insights into the multipolarity of emitted gamma rays and assist in assigning spin and parity to newly discovered nuclear states.

The analysis of the $LaBr_3$(Ce) detectors data will allow the extraction of half-lives for excited states in ^{62}Fe. This data will facilitate precise calculations of the reduced transition rates for transitions that depopulate these levels. Such calculations provide insights into the degree of collectivity in these transitions and the characteristics of the nucleus.

Chapter 7
Appendix

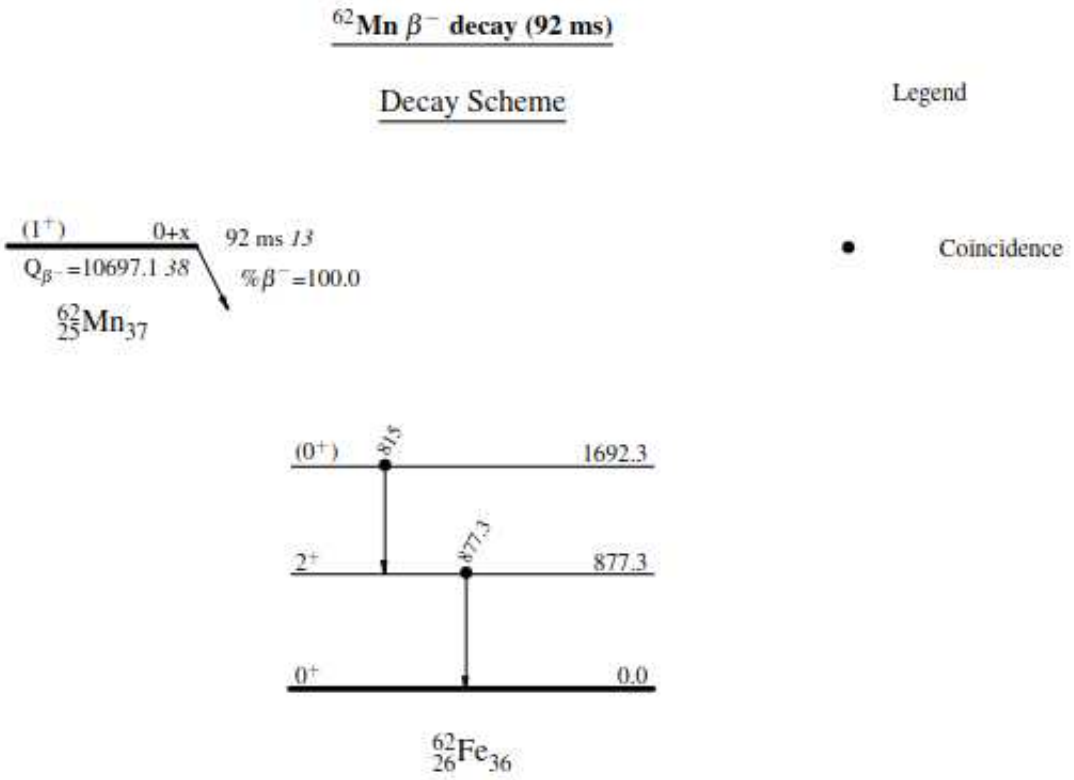

Figure 7.1: *The level scheme of* ^{62}*Fe from the decay of* 1^+ *isomers of* ^{62}*Mn studied by [Hoteling et al., 2010]. This level scheme information is sourced from the NNDC [nnd,]*

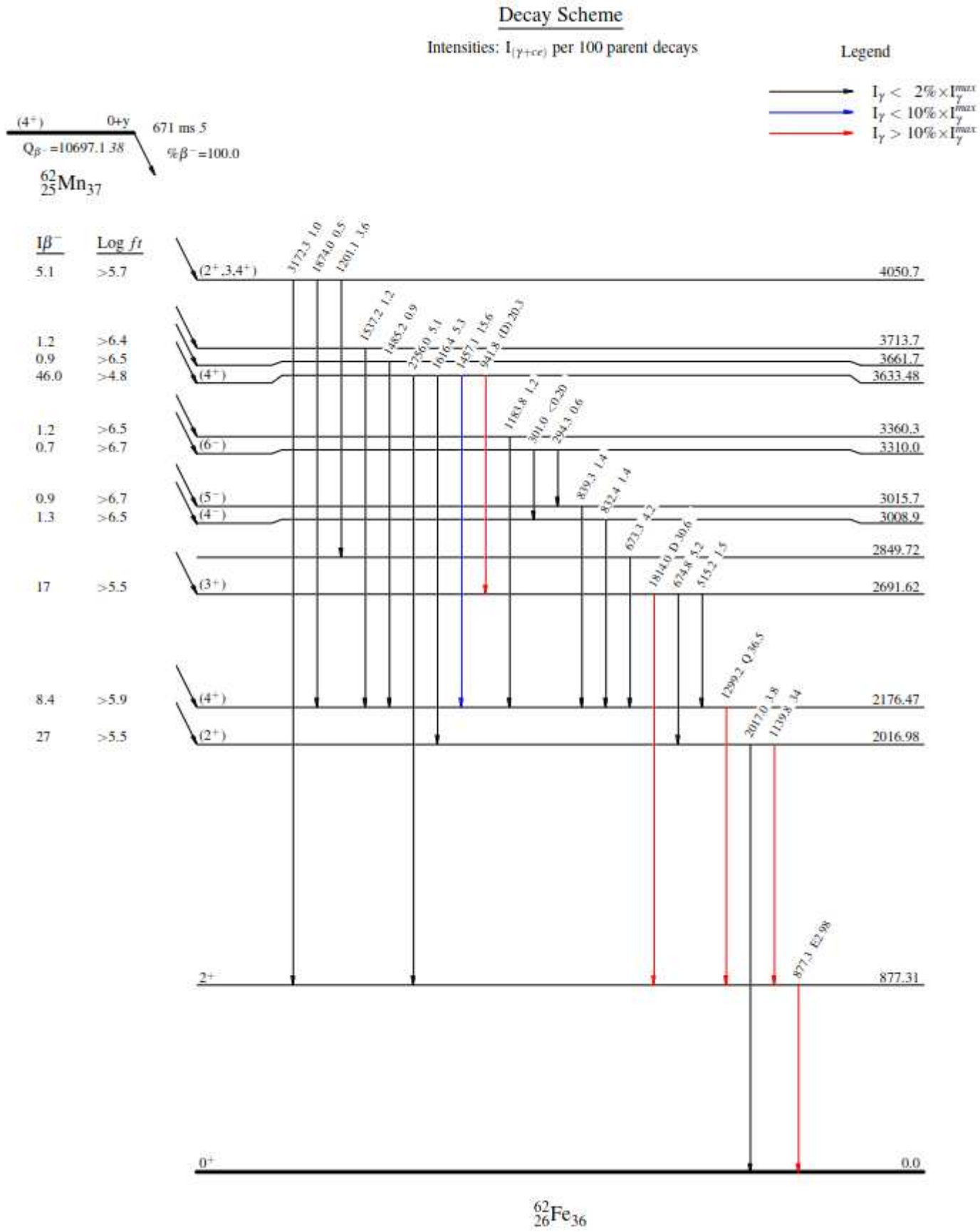

Figure 7.2: *The level scheme of ^{62}Fe from the decay of 4^+ isomers of ^{62}Mn studied by [Hoteling et al., 2010]. This level scheme information is sourced from the NNDC [nnd,]*

Table 7.1: *All the bins are tabulated here. The address is actually the cable that connects the detector to the DAQ. The bins that were not working are highlighted in red.*

Bin Number	Address	Bin Number	Address
1	0x0	33	0x1000
2	0x1	34	0x1001
3	0x2	35	0x1002
4	0x3	36	0x1003
5	0x200	37	0x1200
6	0x201	38	0x1201
7	0x202	39	0x1202
8	0x203	40	0x1203
9	0x400	41	0x1400
10	0x401	42	0x1401
11	0x402	43	0x1402
12	0x403	44	0x1403
13	0x600	45	0x1600
14	0x601	46	0x1601
15	0x602	47	0x1602
16	0x603	48	0x1603
17	0x800	49	0x1800
18	0x801	50	0x1801
19	0x802	51	0x1802
20	0x803	52	0x1803
21	0xa00	53	0x1a00
22	0xa01	54	0x1a01
23	0xa02	55	0x1a02
24	0xa03	56	0xa03
25	0xc00	57	0x1c00
26	0xc01	58	0x1c01
27	0xc02	59	0x1c02
28	0xc03	60	0x1c03
29	0xe00	61	0x1e00
30	0xe01	62	0x1e01
31	0xe02	63	0x1e02
32	0xe03	64	0x1e03

Bibliography

[fey,] Feynman diagrams. https://digestiblenotes.com/physics/fundamental_particles/feynman_diagrams.php.

[ged,] Ge detector. https://www.physics.uoguelph.ca/griffin.

[grs,] Grsisort. https://github.com/GRIFFINCollaboration/GRSISort#grsisort.

[int,] Interaction with matter. https://www.fe.infn.it/radioactivity/educational/detection.html.

[log,] log. https://www.nndc.bnl.gov/logft/.

[mag,] Magic numbers. http://ne.phys.kyushu-u.ac.jp/seminar/MicroWorld3_E/3Part2_E/3P25_E/magic_numbers_E.htm. Accessed: Insert Date.

[nnd,] Nuclear chart. https://www.nndc.bnl.gov/nudat3/.

[Adrich et al., 2008] Adrich, P., Amthor, A., Bazin, D., Bowen, M., Brown, B., Campbell, C., Cook, J., Gade, A., Galaviz, D., Glasmacher, T., et al. (2008). In-beam γ-ray spectroscopy and inclusive two-proton knockout cross section measurements at n 40. *Physical Review C*, 77(5):054306.

[Alburger et al., 1964] Alburger, D., Chasman, C., Jones, K., Olness, J., and Ristinen, R. (1964). Parity of be 11. *Physical Review*, 136(4B):B916.

[Anwer Ahmed, 2015] Anwer Ahmed, M. A.-S. (2015). *Nuclear shell structure of odd-a magnesium isotopes within USDA Hamiltonian/Anwer Ahmed Mohammed Al-Sammarraie*. PhD thesis, Universiti Malaya.

[Baartman, 2014] Baartman, R. (2014). Isac lebt. *ISAC and ARIEL: The TRIUMF Radioactive Beam Facilities and the Scientific Program*, pages 69–77.

[Bäckman et al., 1985] Bäckman, S.-O., Brown, G. E., and Niskanen, J. A. (1985). The nucleon-nucleon interaction and the nuclear many-body problem. *Physics Reports*, 124(1):1–68.

[Ball et al., 2005] Ball, G., Achtzehn, T., Albers, D., Al Khalili, J., Andreoiu, C., Andreyev, A., Ashley, S., Austin, R., Becker, J., Bricault, P., et al. (2005). High-resolution γ-ray spectroscopy: a versatile tool for nuclear β-decay studies at triumf-isac. *Journal of physics G: Nuclear and particle physics*, 31(10):S1491.

[Bansal and French, 1964] Bansal, R. and French, J. (1964). Even-parity-hole states in f72-shell nuclei. *Physics Letters*, 11(2):145–148.

[Bastin et al., 2007] Bastin, B., Grévy, S., Sohler, D., Sorlin, O., Dombrádi, Z., Achouri, N., Angélique, J., Azaiez, F., Baiborodin, D., Borcea, R., et al. (2007). Collapse of the n= 28 shell closure in s 42 i. *Physical review letters*, 99(2):022503.

[Bernas et al., 1991] Bernas, M., Armbruster, P., Czajkowski, S., Faust, H., Bocquet, J., and Brissot, R. (1991). Discovery of neutron-rich co and fe isotopes in pu 239 (n th, f): Yields and half-lives. *Physical review letters*, 67(26):3661.

[Bernas et al., 1982] Bernas, M., Dessagne, P., Langevin, M., Payet, J., Pougheon, F., and Roussel, P. (1982). Magic features of 68ni. *Physics Letters B*, 113(4):279–282.

[Bertsch et al., 1977] Bertsch, G., Borysowicz, J., McManus, H., and Love, W. (1977). Interactions for inelastic scattering derived from realistic potentials. *Nuclear Physics A*, 284(3):399–419.

[Blackmore, 2000] Blackmore, E. W. (2000). Operation of the triumf (20-500 mev) proton irradiation facility. In *2000 IEEE Radiation Effects Data Workshop. Workshop Record. Held in conjunction with IEEE Nuclear and Space Radiation Effects Conference (Cat. No. 00TH8527)*, pages 1–5. IEEE.

[Broda et al., 1995] Broda, R., Fornal, B., Królas, W., Pawłat, T., Bazzacco, D., Lunardi, S., Rossi-Alvarez, C., Menegazzo, R., De Angelis, G., Bednarczyk, P., et al. (1995). N= 40 neutron subshell closure in the ni 68 nucleus. *Physical Review Letters*, 74(6):868.

[Brown, 2005] Brown, B. A. (2005). Lecture notes in nuclear structure physics. *National Super Conducting Cyclotron Laboratory*, 11.

[Brown, 2010] Brown, B. A. (2010). Islands of insight in the nuclear chart. *Physics*, 3:104.

[Brun and Rademakers, 1997] Brun, R. and Rademakers, F. (1997). Root—an object oriented data analysis framework. *Nuclear instruments and methods in physics research section A: accelerators, spectrometers, detectors and associated equipment*, 389(1-2):81–86.

[Bryan, 2023] Bryan, J. C. (2023). *Introduction to nuclear science*. CRC Press.

[Daugas et al., 2011] Daugas, J., Matea, I., Delaroche, J.-P., Pfützner, M., Sawicka, M., Becker, F., Bélier, G., Bingham, C., Borcea, R., Bouchez, E., et al. (2011). β-decay measurements for n¿ 40 mn nuclei and inference of collectivity for neutron-rich fe isotopes. *Physical Review C*, 83(5):054312.

[Dilling et al., 2014] Dilling, J., Krücken, R., and Merminga, L. (2014). *ISAC and ARIEL: the TRIUMF radioactive beam facilities and the scientific program*. Springer.

[Dobaczewski et al., 1994] Dobaczewski, J., Hamamoto, I., Nazarewicz, W., and Sheikh, J. (1994). Nuclear shell structure at particle drip lines. *Physical review letters*, 72(7):981.

[Fraile-Prieto et al., 2008] Fraile-Prieto, L., Nyberg, J., Turrin, M., Udias, J., Baluyut, A., Korgul, A., Fynbo, H., Aprahamian, A., Kurcewicz, W., Bucher, M., et al. (2008). Fast-timing studies of nuclei below ˆ{68} ni populated in the β-decay of mn isotopes. Technical report.

[Garnsworthy et al., 2019] Garnsworthy, A., Svensson, C., Bowry, M., Dunlop, R., MacLean, A., Olaizola, B., Smith, J., Ali, F., Andreoiu, C., Ash, J., et al. (2019). The griffin facility for decay-spectroscopy studies at triumf-isac. *Nuclear Instruments and Methods in Physics Research Section A: Accelerators, Spectrometers, Detectors and Associated Equipment*, 918:9–29.

[Garrett, 2014] Garrett, P. (2014). Descant–the deuterated scintillator array for neutron tagging. *ISAC and ARIEL: The TRIUMF Radioactive Beam Facilities and the Scientific Program*, pages 137–141.

[Gaudefroy et al., 2009] Gaudefroy, L., Obertelli, A., Péru, S., Pillet, N., Hilaire, S., Delaroche, J.-P., Girod, M., and Libert, J. (2009). Collective structure of the n= 40 isotones. *Physical Review C*, 80(6):064313.

[Gaudefroy et al., 2005] Gaudefroy, L., Sorlin, O., Donzaud, C., Angélique, J., Azaiez, F., Bourgeois, C., Chiste, V., Dlouhy, Z., Grévy, S., Guillemaud-Mueller, D., et al. (2005). Beta-decay studies of neutron-rich sc-cr nuclei. *The European Physical Journal A-Hadrons and Nuclei*, 23:41–48.

[Gove and Martin, 1971] Gove, N. and Martin, M. (1971). Log-f tables for beta decay. *Atomic Data and Nuclear Data Tables*, 10(3):205–219.

[Grawe et al., 2001] Grawe, H., Górska, M., Döring, J., Fahlander, C., Palacz, M., Nowacki, F., Caurier, E., Daugas, J., Lewitowicz, M., Sawicka, M., et al. (2001). Tours symposium on nuclear physics iv, tours 2000.

[Greiner and Reinhardt, 1996] Greiner, W. and Reinhardt, J. (1996). *Field quantization*. Springer Science & Business Media.

[Grotz and Klapdor, 1990] Grotz, K. and Klapdor, H. V. (1990). *The weak interaction in nuclear, particle and astrophysics*. CRC Press.

[Grzywacz et al., 1998] Grzywacz, R., Béraud, R., Borcea, C., Emsallem, A., Glogowski, M., Grawe, H., Guillemaud-Mueller, D., Hjorth-Jensen, M., Houry, M., Lewitowicz, M., et al. (1998). New island of μ s isomers in neutron-rich nuclei around the z= 28 and n= 40 shell closures. *Physical review letters*, 81(4):766.

[Hackman and Svensson, 2014] Hackman, G. and Svensson, C. (2014). The triumf-isac gamma-ray escape suppressed specrometer, tigress. *Hyperfine Interactions*, 225:241–251.

[Hannawald et al., 1999] Hannawald, M., Kautzsch, T., Wöhr, A., Walters, W., Kratz, K.-L., Fedoseyev, V., Mishin, V., Böhmer, W., Pfeiffer, B., Sebastian, V., et al. (1999). Decay of neutron-rich mn nuclides and deformation of heavy fe isotopes. *Physical review letters*, 82(7):1391.

[Hoteling et al., 2010] Hoteling, N., Chiara, C., Broda, R., Walters, W., Janssens, R., Hjorth-Jensen, M., Carpenter, M., Fornal, B., Hecht, A., Królas, W., et al. (2010). Structure of fe 60, 62 and the onset of ν g 9/2 occupancy. *Physical Review C*, 82(4):044305.

[Khandaker, 2011] Khandaker, M. U. (2011). High purity germanium detector in gamma-ray spectrometry: High-purity germanium detector. *International Journal of Fundamental Physical Sciences*, 1(2):42–46.

[Knoll, 2010] Knoll, G. F. (2010). *Radiation detection and measurement*. John Wiley & Sons.

[Krane, 1991] Krane, K. S. (1991). *Introductory nuclear physics*. John Wiley & Sons.

[Kunz et al., 2023] Kunz, P., Lassen, J., Andreoiu, C., Garcia, F. H., Yang, H., and Radchenko, V. (2023). Understanding radioactive ion beam production at isac through yield measurements and simulations. *Nuclear Instruments and Methods in Physics Research Section B: Beam Interactions with Materials and Atoms*, 541:117–120.

[Lee, 1990] Lee, I.-Y. (1990). The gammasphere. *Nuclear Physics A*, 520:c641–c655.

[Lenzi et al., 2010] Lenzi, S. M., Nowacki, F., Poves, A., and Sieja, K. (2010). Island of inversion around cr 64. *Physical Review C*, 82(5):054301.

[Li, 2023] Li, J. (2023). Merging of the island of inversion at n= 40 and n= 50. *Physics Letters B*, 840:137893.

[Ljungvall et al., 2010] Ljungvall, J., Görgen, A., Obertelli, A., Korten, W., Clément, E., De France, G., Bürger, A., Delaroche, J.-P., Dewald, A., Gadea, A., et al. (2010). Onset of collectivity in neutron-rich fe isotopes: Toward a new island of inversion? *Physical Review C*, 81(6):061301.

[Mayer, 1949] Mayer, M. G. (1949). On closed shells in nuclei. ii. *Physical Review*, 75(12):1969.

[Naimi et al., 2012] Naimi, S., Audi, G., Beck, D., Blaum, K., Böhm, C., Borgmann, C., Breitenfeldt, M., George, S., Herfurth, F., Herlert, A., et al. (2012). Surveying the n= 40 island of inversion with new manganese masses. *Physical Review C*, 86(1):014325.

[Navin et al., 2000] Navin, A., Anthony, D., Aumann, T., Baumann, T., Bazin, D., Blumenfeld, Y., Brown, B., Glasmacher, T., Hansen, P., Ibbotson, R., et al. (2000). Direct evidence for the breakdown of the n= 8 shell closure in b 12 e. *Physical review letters*, 85(2):266.

[Nowacki et al., 2016] Nowacki, F., Poves, A., Caurier, E., and Bounthong, B. (2016). Shape coexistence in ni 78 as the portal to the fifth island of inversion. *Physical review letters*, 117(27):272501.

[Osterfeld, 1992] Osterfeld, F. (1992). Nuclear spin and isospin excitations. *Reviews of Modern Physics*, 64(2):491.

[Otsuka, 2002] Otsuka, T. (2002). Shell, shape and spin/isospin structures of exotic nuclei. *Progress of Theoretical Physics Supplement*, 146:6–15.

[Otsuka et al., 2001] Otsuka, T., Fujimoto, R., Utsuno, Y., Brown, B. A., Honma, M., and Mizusaki, T. (2001). Magic numbers in exotic nuclei and spin-isospin properties of the nn interaction. *Physical Review Letters*, 87(8):082502.

[Otsuka et al., 2020] Otsuka, T., Gade, A., Sorlin, O., Suzuki, T., and Utsuno, Y. (2020). Evolution of shell structure in exotic nuclei. *Reviews of modern physics*, 92(1):015002.

[Otsuka et al., 2005] Otsuka, T., Suzuki, T., Fujimoto, R., Grawe, H., and Akaishi, Y. (2005). Evolution of nuclear shells due to the tensor force. *Physical Review Letters*, 95(23):232502.

[Pauwels et al., 2008] Pauwels, D., Ivanov, O., Bree, N., Büscher, J., Cocolios, T. E., Gentens, J., Huyse, M., Korgul, A., Kudryavtsev, Y., Raabe, R., et al. (2008). Shape isomerism at n= 40: Discovery of a proton intruder state in co 67. *Physical Review C*, 78(4):041307.

[Pauwels et al., 2009] Pauwels, D., Ivanov, O., Bree, N., Büscher, J., Cocolios, T. E., Huyse, M., Kudryavtsev, Y., Raabe, R., Sawicka, M., Van de Walle, J., et al. (2009). Structure of co 65, 67 studied through the β decay of fe 65, 67 and a deep-inelastic reaction. *Physical Review C*, 79(4):044309.

[Pudliner et al., 1997] Pudliner, B., Pandharipande, V., Carlson, J., Pieper, S. C., and Wiringa, R. B. (1997). Quantum monte carlo calculations of nuclei with a¡˜ 7. *Physical Review C*, 56(4):1720.

[Raeder et al., 2013] Raeder, S., Dombsky, M., Heggen, H., Lassen, J., Quenzel, T., Sjödin, M., Teigelhöfer, A., and Wendt, K. (2013). In-source laser spectroscopy developments at trilis—towards spectroscopy on actinium and scandium. *Hyperfine Interactions*, 216:33–39.

[Rizwan et al., 2016] Rizwan, U., Garnsworthy, A., Andreoiu, C., Ball, G., Chester, A., Domingo, T., Dunlop, R., Hackman, G., Rand, E., Smith, J., et al. (2016). Characteristics of griffin high-purity germanium clover detectors. *Nuclear Instruments and Methods in Physics Research Section A: Accelerators, Spectrometers, Detectors and Associated Equipment*, 820:126–131.

[Runte et al., 1983] Runte, E., Schmidt-Ott, W.-D., Tidemand-Petersson, P., Kirchner, R., Klepper, O., Kurcewicz, W., Roeckl, E., Kaffrell, N., Peuser, P., Rykaczewski, K., et al. (1983). Decay studies of neutron-rich products from 76ge induced multinucleon transfer reactions including the new isotopes 62mn, 63fe and 71, 72, 73cu. *Nuclear Physics A*, 399(1):163–180.

[Siegbahn and Axel, 1966] Siegbahn, K. and Axel, P. (1966). Alpha-, beta-, and gamma-ray spectroscopy. *American Journal of Physics*, 34(3):275–276.

[Sorlin et al., 1999] Sorlin, O., Donzaud, C., Axelsson, L., Belleguic, M., Béraud, R., Borcea, C., Canchel, G., Chabanat, E., Daugas, J., Emsallem, A., et al. (1999). Beta decay half-lives of neutron rich ti–co isotopes around n= 40. *Nuclear Physics A*, 660(1):3–19.

[Sorlin et al., 2003a] Sorlin, O., Donzaud, C., Azaiez, F., Bourgeois, C., Gaudefroy, L., Ibrahim, F., Guillemaud-Mueller, D., Pougheon, F., Lewitowicz, M., de Oliveira Santos, F., et al. (2003a). Beta decay studies of neutron-rich 21sc 27co nuclei at ganil. *Nuclear Physics A*, 719:C193–C200.

[Sorlin et al., 2003b] Sorlin, O., Donzaud, C., Nowacki, F., Angélique, J., Azaiez, F., Bourgeois, C., Chiste, V., Dlouhy, Z., Grévy, S., Guillemaud-Mueller, D., et al. (2003b). New region of deformation in the neutron-rich 60 24 cr 36 and 62 24 cr 38. *The European Physical Journal A-Hadrons and Nuclei*, 16:55–61.

[Sorlin et al., 2002] Sorlin, O., Leenhardt, S., Donzaud, C., Duprat, J., Azaiez, F., Nowacki, F., Grawe, H., Dombrádi, Z., Amorini, F., Astier, A., et al. (2002). N 28 68 i 40: Magicity versus superfluidity. *Physical Review Letters*, 88(9):092501.

[Stanoiu et al., 2008] Stanoiu, M., Sohler, D., Sorlin, O., Azaiez, F., Dombrádi, Z., Brown, B., Belleguic, M., Borcea, C., Bourgeois, C., Dlouhy, Z., et al. (2008). Disappearance of the n= 14 shell gap in the carbon isotopic chain. *Physical Review C*, 78(3):034315.

[Svensson and Garnsworthy, 2014] Svensson, C. and Garnsworthy, A. (2014). The griffin spectrometer. *Hyperfine Interactions*, 225:127–132.

[Thibault et al., 1975] Thibault, C., Klapisch, R., Rigaud, C., Poskanzer, A., Prieels, R., Lessard, L., and Reisdorf, W. (1975). Direct measurement of the masses of li 11 and na 2 6- 3 2 with an on-line mass spectrometer. *Physical Review C*, 12(2):644.

[Tsunoda et al., 2014] Tsunoda, Y., Otsuka, T., Shimizu, N., Honma, M., and Utsuno, Y. (2014). Novel shape evolution in exotic ni isotopes and configuration-dependent shell structure. *Physical Review C*, 89(3):031301.

[Turkat et al., 2023] Turkat, S., Mougeot, X., Singh, B., and Zuber, K. (2023). Systematics of log ft values for β-, and ec/β+ transitions. *Atomic Data and Nuclear Data Tables*, page 101584.

[Yukawa, 1935] Yukawa, H. (1935). On the interaction of elementary particles. i. *Proceedings of the Physico-Mathematical Society of Japan. 3rd Series*, 17:48–57.